CrossMark

The Orbital Eccentricities of Directly Imaged Companions Using Observable-based Priors: Implications for Population-level Distributions

Clarissa R. Do Ó[1] , Kelly K. O'Neil[2] , Quinn M. Konopacky[1] , Tuan Do[2] , Gregory D. Martinez[2],
Jean-Baptiste Ruffio[1] , and Andrea M. Ghez[2]
[1] Center for Astrophysics and Space Sciences, University of California, San Diego, La Jolla, CA 92093, USA
[2] Department of Physics and Astronomy, University of California, Los Angeles, Los Angeles, CA 90095, USA

Abstract

The eccentricity of a substellar companion is an important tracer of its formation history. Directly imaged companions often present poorly constrained eccentricities. A recently developed prior framework for orbit fitting called "observable-based priors" has the advantage of improving biases in derived orbit parameters for objects with minimal phase coverage, which is the case for the majority of directly imaged companions. We use observable-based priors to fit the orbits of 21 exoplanets and brown dwarfs in an effort to obtain the eccentricity distributions with minimized biases. We present the objects' individual posteriors compared to their previously derived distributions, showing in many cases a shift toward lower eccentricities. We analyze the companions' eccentricity distribution at a population level, and compare this to the distributions obtained with the traditional uniform priors. We fit a Beta distribution to our posteriors using observable-based priors, obtaining shape parameters $\alpha = 1.09^{+0.30}_{-0.22}$ and $\beta = 1.42^{+0.33}_{-0.25}$. This represents an approximately flat distribution of eccentricities. The derived α and β parameters are consistent with the values obtained using uniform priors, though uniform priors lead to a tail at high eccentricities. We find that separating the population into high- and low-mass companions yields different distributions depending on the classification of intermediate-mass objects. We also determine via simulation that the minimal orbit coverage needed to give meaningful posteriors under the assumptions made for directly imaged planets is ≈15% of the inferred period of the orbit.

1. Introduction

The field of exoplanet direct imaging has advanced significantly in recent years, with the detection capabilities of ground-based telescopes improving due to technological developments in adaptive optics (AO). Direct imaging also allows for the measurement of the relative astrometry of planets over time, which can in turn allow astronomers to better constrain the orbital parameters of these objects and the overall orbital architecture of their systems. By better understanding the architecture of these extrasolar systems, we may obtain an understanding of formation pathways of planetary systems in our galaxy. Thus, orbit fitting of directly imaged exoplanets has the potential to shed light on the early formation history and dynamical evolution of planetary systems with widely separated, gas giant planets.

In particular, the eccentricity of a planet can tell us much about how it was formed. In the theory of protoplanetary disk formation, disk fluid elements can initially be in an eccentric orbit, but soon lose energy through collisions and settle into the minimum energy orbit, which is a circular orbit (Lodato 2008). Therefore, planets forming in a protoplanetary disk via core or pebble accretion should have lower eccentricities, but can develop higher eccentricities through processes such as planet–planet scattering or disk migration (Papaloizou & Terquem 2006;

Chatterjee et al. 2008; Dong & Dawson 2016; Johansen & Lambrechts 2017; Bowler et al. 2020). Various protoplanetary disk processes can also either damp eccentricities (e.g., Kley & Nelson 2012; Bitsch & Kley 2010) or excite eccentricities (e.g., Moorhead & Adams 2008; Goldreich & Sari 2003). Formation of planets via gravitational instability can potentially form planets with higher eccentricities. Generally, planet formation via gravitational instability occurs farther from the host star, causing eccentricity damping timescales to be longer at such large separations (e.g., Mayer et al. 2004). These various processes may lead to a variety of eccentricities for individual planetary systems, so it is difficult to tell which mechanism is operating for individual systems. However, the eccentricity distribution of many planetary systems (i.e., the parent distribution) can give us strong constraints on which formation mechanisms are at work. Planets that slowly form from protoplanetary disks in unperturbed orbits should have low eccentricities, while planets that undergo planetary migration or outward scattering can have a range of varying eccentricities.

Efforts to obtain an eccentricity distribution at a population level for substellar companions have already been made for a number of exoplanet and brown dwarf populations. Hogg et al. (2010) presented the method of hierarchical Bayesian modeling to obtain parameters for the underlying parent eccentricity distribution from the posteriors of exoplanet parameters given from orbital fits. The planet population simulated by Hogg et al. (2010) was inferred from radial velocity (RV) measurements of hot Jupiters. Kipping (2013) constrained eccentricity distributions of short-period exoplanets using data obtained

from 396 companions using the RV method. Bowler et al. (2020) used data from 27 long-period, directly imaged companions to obtain an eccentricity distribution of these objects. They found that extrasolar companions present different eccentricity distributions if they are low mass or high mass. They conclude that "exoplanets," or lower-mass companions, have lower eccentricities (so they likely formed from a disk) and "brown dwarfs," or higher-mass companions, have higher eccentricities (consistent with binary star formation). This conclusion, if true, is groundbreaking—it suggests that these companions can be observationally distinguished via their eccentricities. In this work, we revisit this analysis using a different set of priors and modified sample of directly imaged substellar companions.

In order to determine the orbital eccentricities of exoplanets, the standard procedure is to fit astrometric data of the companion relative to the star at different points in time using Bayesian statistics. Within the Bayesian framework, prior probability distributions (priors) for each orbit parameter must be assumed to ultimately infer posterior probability distributions (posteriors) for each parameter. The most common priors assumed for orbital parameters are model-based priors (i.e., they assume a prior distribution in the six model parameters of a Keplerian orbit). They generally assume distributions that are uniform (for the eccentricity, argument of periastron, and period of ascending nodes), log-uniform (semimajor axis) and sine (inclination). It is also common practice to narrow down the parameter space with physically motivated priors, such as stability constraints, coplanarity and stellar rotation rates (e.g., Pearce et al. 2015; Wang et al. 2018; Wang et al. 2020; Thompson et al. 2023; Yimiao Zhang et al. 2023). However, for orbits where less than 40% of the orbital arc is covered, which is the majority of directly imaged companions, this standard method of model-based priors (which herein we will refer to as "uniform" priors, as is done by O'Neil et al. 2019) has been shown to introduce biases in the resulting posterior distributions, generating inaccurate parameters and confidence intervals (Lucy 2014; Martinez et al. 2017). The eccentricity parameter is generally affected by this issue, with many objects presenting a bias toward high eccentricities when fit with uniform priors.

O'Neil et al. (2019) presented a new approach to priors for the orbit fitting of long-period resolved companions, which is based on uniformity in the observable parameters rather than in the model parameters. This approach is called "observable-based" priors. This method has been shown to reduce this bias in orbital parameters where the orbital arc of the object is less than 40% covered. In this work, we aim to obtain the eccentricity distribution of extrasolar companions at a population level, using observable-based priors to fit the orbits of 21 directly imaged companions. Given that the majority of our substellar companion sample is undersampled (i.e., their current orbital coverage spans a small amount of their orbital arc), we also perform a series of simulations to assess the minimum orbital coverage needed in order to get meaningful eccentricity posteriors for directly imaged companions.

Our analysis is outlined as follows. We introduce our sample and present the astrometric and RV data used for our orbit fits in Sections 2.1 and 2.2. In Section 3.1, we present the concept of observable-based priors. We present our results in Section 4, describing the results of our orbit fitting of the 21 companions (Section 4.1) and simulations for the minimal orbital coverage

needed (Section 4.2). We discuss the implications of our work in Section 5 and our conclusions in Section 6.

2. Data

2.1. Sample Selection and Astrometric Data

The companions chosen are a subsample of objects from Bowler et al. (2020). The criteria for choosing these objects are outlined in detail in Bowler et al. (2020); we summarize them here: the objects must be at a projected separation of 5–100 au from the host star at the time of discovery, and the hosts must be stars ($M > 75\ M_{\rm Jup}$), such that any companions that are clearly part of binary systems are excluded from the sample. For the systems with more than one detected planet, such as HR 8799, PDS 70, HD 206893, and β Pictoris, we chose only one planet as the "representative" of the system's eccentricity in this analysis. We made this choice so that multiple planets from the same system would not bias our resulting eccentricity distributions, since it has been shown that planets with multiple systems present lower eccentricities due to stability requirements (Wright et al. 2009), and therefore the eccentricities within a single system are correlated. We also do not include any companions that have less than four epochs of observation, as our software requires this value as a minimum amount of astrometry for orbit fitting given the number of free parameters. With these requirements, 21 companions are in the sample used in this work. The sample is presented in Table 1.

The astrometry used, as well as a fixed total system mass and distance, include points up to 2018 from Bowler et al. (2020), as well as updated data from the literature for eight of the companions. The new astrometry points used are presented in Table 2. The astrometry from Bowler et al. (2020) includes points from the literature for HD 984 b (Meshkat et al. 2015; Johnson-Groh et al. 2017), HD 1160 b (Nielsen et al. 2012; Maire et al. 2016; Currie et al. 2018), HD 19467 B (Crepp et al. 2014; Crepp et al. 2015), 1RXS0342+1216 b (Janson et al. 2012; Bowler et al. 2014; Janson et al. 2014; Bowler et al. 2015), 51 Eri b (Maire et al. 2019), HD 49197 b (Metchev & Hillenbrand 2005; Serabyn et al. 2009; Bottom et al. 2016), HR 2562 b (Konopacky et al. 2016b; Maire et al. 2018), HR 3549 b (Mawet et al. 2015; Mesa et al. 2016), HD 95086 b (Rameau et al. 2016; Chauvin et al. 2018), GJ 504 b (Kuzuhara et al. 2013; Bonnefoy et al. 2018), HIP 65426 b (Chauvin et al. 2017b; Cheetham et al. 2019), Müller et al. 2018; Wagner et al. 2018), PZ Tel b (Biller et al. 2010; Mugrauer et al. 2012; Ginski et al. 2014; Beust et al. 2016; Maire et al. 2016), HD 206893 b (Milli et al. 2016; Delorme et al. 2017; Grandjean et al. 2019), κ And B (Carson et al. 2013; Currie et al. 2018), Bryan et al. 2016), HD 4747 b (Brandt et al. 2019), Gl 229 b (Brandt et al. 2019), HR 7672 b (Brandt et al. 2019), Gl 758 b (Brandt et al. 2019), and HR 8799c (Konopacky et al. 2016a; Wang et al. 2018).

2.2. Radial Velocity Data

Relative RVs, when available, contribute a great deal of information to visual orbit fits. Since RV measurements are challenging to obtain for directly imaged companions, only six objects in this study have RVs available in the literature. The RVs used are shown in Table 3.

Using RVs for these six objects allows us to eliminate the degeneracy in Ω and therefore better constrain the orbital plane of the object. Additionally, using RV data for HD 1160 b

Table 1
Companions in the Sample

Object	Inferred Mass (M_J)	Mass Classification	Primary Spectral Type	Age (Myr)	Average Separation (as; au)	References
51 Eri b	2.6 ± 0.3	Giant Planet	F0IV	20^{+6}_{-6}	0.45; 13.2	1; 2; 3
GJ 504 b	$4.0^{+4.5}_{-1.0}$	Giant Planet	G0	160^{+350}_{-60}	2.5; 43.5	4
HD 95086 b	2.6 ± 0.4	Giant Planet	A8	17^{+4}_{-4}	4.5; 56	1; 5
PDS 70 c	4.4 ± 1.1	Giant Planet	K7	$5.4^{+1.0}_{-1.0}$	0.2; 30.2	6; 7
HR 8799c	8.3 ± 0.6	Giant Planet	A5V	30^{+20}_{-10}	0.7; 38	1; 8
HIP 65426 b	7.1 ± 1.1	Giant Planet	A2V	14^{+4}_{-4}	0.82; 86	9; 10
κ And b	13^{+12}_{-2}	Boundary	B9V	47^{+27}_{-40}	0.91; 76.5	11; 12
β Pic b	$11.9^{+2.93}_{-3.04}$	Boundary	A6V	22^{+3}_{-3}	0.25; 9.9	13; 14; 15
HR 2562 b	$10.28^{+5.00}_{-5.00}$	Boundary	F5V	600^{+300}_{-300}	0.618; 20.3	16; 17
HD 206893 b	$28.00^{+2.2}_{-2.1}$	Brown Dwarf	F5V	1100^{+1000}_{-1000}	0.27; 10	18; 19
1RXS0342+1216 b	35 ± 8	Brown Dwarf	M4	60–300	0.83; 19.8	20
Gl 758 b	37.9 ± 1.5	Brown Dwarf	K0V	8200^{+500}_{-500}	1.6; 25	21; 22; 35
HR 3549 b	45 ± 5	Brown Dwarf	A0V	100–500	0.9; 83.2	23
HD 1160 b	33^{+12}_{-9}	Brown Dwarf	A0V	80–120	0.78; 81	24; 25
HD 19467 b	52 ± 4.3	Brown Dwarf	G3V	4600–10,000	1.65; 51.1	26
HR 7672 b	61.5 ± 6.5	Brown Dwarf	G1V	1000–3000	0.79; 14	27
PZ Tel b	64 ± 5	Brown Dwarf	G9IV	23^{+3}_{-3}	0.50; 23.65	1; 15
Gl 229 b	35 ± 15	Brown Dwarf	M1V	7000–10,000	6.03; 34.7	28; 29; 30
HD 4747 b	66.6 ± 3.5	Brown Dwarf	G9V	3300^{+2300}_{-1900}	0.6; 11.3	31; 32
HD 984 b	61 ± 4	Brown Dwarf	F7V	80^{+120}_{-50}	0.22; 28	33
HD 49197 b	$63.2^{+12.6}_{-26.32}$	Brown Dwarf	F5V	290-790	0.95; 44	34

References. (1) Nielsen et al. (2019); (2) Bell et al. (2015); (3) Macintosh et al. (2015); (4) Kuzuhara et al. (2013); (5) Meshkat et al. (2013); (6) Mesa et al. (2019); (7) Keppler et al. (2018); (8) Marois et al. (2010); (9) Carter et al. (2022); (10) Chauvin et al. (2017a); (11) Currie et al. (2018); (12) Jones et al. (2016); (13) Lacour et al. (2021); (14) Gray et al. (2006); (15) Mamajek & Bell (2014); (16) Yimiao Zhang et al. (2023); (17) Konopacky et al. (2016a); (18) Hinkley et al. (2023); (19) Milli et al. (2016); (20) Bowler et al. (2014); (21) Brandt et al. (2019); (22) Mamajek & Hillenbrand (2008); (23) Mesa et al. (2016); (24) Nielsen et al. (2012); (25) Garcia et al. (2017); (26) Jensen-Clem et al. (2016); (27) Liu et al. (2002); (28) Nakajima et al. (1995); (29) Byrne et al. (1985); (30) Brandt et al. (2020); (31) Xuan & Wyatt (2020); (32) Crepp et al. (2016); (33) Franson et al. (2022); (34) Metchev & Hillenbrand (2005); (35) Bowler et al. (2018).

changed the eccentricity distribution of the companion when using uniform priors (see Section 4.1.2).

3. Methods

3.1. Orbit Fitting

We use observable-based priors for fitting the relative astrometry to orbits for all 21 directly imaged companions. These priors are implemented in the orbit fitting software Efit5 (Meyer et al. 2012). Efit5 uses MULTINEST (Feroz & Hobson 2008; Feroz et al. 2009), a multimodal (or nested) sampling algorithm, to perform a Bayesian analysis on the data. For all of these fits, we use 3000 live points in the nested sampling algorithm. We also include relative RVs when available. In order to compare these results to the uniform prior approach, we also fit for the orbits of these companions with uniform priors. For our orbit fitting with uniform priors, we use both the Efit5 package and the orbitize! package (Blunt et al. 2020) with the Markov Chain Monte Carlo approach. We verify that both fitting methods with uniform priors give consistent results. For the uniform priors with orbitize, we fit for 50 million possible orbits, using 1000 walkers, 20 temperatures, 20 threads, 10,000 burn steps, and a thin factor of 10, as is done in Bowler et al. (2020).

After fitting the orbits of the 21 companions using observable-based priors, we use their posteriors to fit for the eccentricity distribution of our entire population of 21 companions. We use a Beta distribution as the model for our parent eccentricity distribution, as is done in other works (e.g., Bowler et al. 2020; Kipping 2013). In order to recover the parent distribution from the sample's posteriors, we use a

maximum likelihood estimate (MLE) fitter in a bootstrapping manner. The details of our recovery technique are presented in Sections 3.2 and 3.3. We then split the sample into subsamples to assess possible distinctions between the population distributions.

The purpose of observable-based priors is to improve orbital estimates for orbits where the data covers a low percentage of the orbital arc ($<40\%$). Here, we briefly summarize the formulation of observable-based priors. A detailed formulation is outlined in O'Neil et al. (2019).

In its general form, observable priors assume that all regions of observable parameter space that can be observed are equally likely, thus emphasizing uniformity in observables rather than in model parameters. In the case of orbit fitting, our fit starts with measured observables D from the astrometry:

$$D = \{x(t), y(t)\} \tag{1}$$

or, for astrometry and RVs:

$$D = \{x(t), y(t), v_z(t)\} \tag{2}$$

where x and y are the object's positions (R.A. and decl.) in the plane of the sky relative to the position of the primary (x_o and y_o), and v_z is the velocity relative to the star. These measured observables are linearly related to the orbital observables (which describe the position and motion in the orbital plane) by the Thiele-Innes constants (e.g Hartkopf et al. 1989; Wright & Howard 2009). Due to this linear relationship, a uniform distribution in the measured observables would imply a uniform distribution in the orbital observables. The orbital observables, denoted here as X, Y, V_x, and V_y, are also

Table 2
Updated Astrometry Points

Object	Epoch	Sep (mas)	PA(°)	Reference
HD 19467 b	2018.793	1631.41.6	238.880.12	Maire et al. (2020)
HIP 65426 b	2018.432	827.26 ± 8.26	149.56 ± 0.55	Stolker et al. (2020)
HD 206893 B	2018.434	269.53 ± 12.15	62.76 ± 2.16	Stolker et al. (2020)
HD 206893 B	2018.679	248.6 ± 4.9	41.8 ± 0.1	Romero et al. (2021)
HD 206893 B	2018.685	248.6 ± 4.9	41.8 ± 0.1	Romero et al. (2021)
HD 206893 B	2018.812	239.12 ± 17.55	42.53 ± 2.17	Stolker et al. (2020)
51 Eri b	2014.961	454.24 ± 1.88	171.22 ± 0.23	De Rosa et al. (2020)
51 Eri b	2015.079	451.81 ± 2.06	170.01 ± 0.26	De Rosa et al. (2020)
51 Eri b	2015.082	456.80 ± 2.57	170.19 ± 0.30	De Rosa et al. (2020)
51 Eri b	2015.085	461.5 ± 23.9	170.4 ± 3.0	De Rosa et al. (2020)
51 Eri b	2015.665	455.10 ± 2.23	167.30 ± 0.26	De Rosa et al. (2020)
51 Eri b	2015.847	452.88 ± 5.41	166.12 ± 0.57	De Rosa et al. (2020)
51 Eri b	2015.961	455.91 ± 6.23	165.66 ± 0.57	De Rosa et al. (2020)
51 Eri b	2015.966	455.01 ± 3.03	165.69 ± 0.43	De Rosa et al. (2020)
51 Eri b	2016.0726	454.46 ± 6.03	165.94 ± 0.51	De Rosa et al. (2020)
51 Eri b	2016.714	454.81 ± 2.02	161.80 ± 0.26	De Rosa et al. (2020)
51 Eri b	2016.722	451.43 ± 2.67	161.73 ± 0.31	De Rosa et al. (2020)
51 Eri b	2016.959	449.39 ± 2.15	160.06 ± 0.27	De Rosa et al. (2020)
51 Eri b	2017.861	447.54 ± 3.02	155.23 ± 0.39	De Rosa et al. (2020)
51 Eri b	2018.884	434.22 ± 2.01	149.64 ± 0.23	De Rosa et al. (2020)
PZ Tel b	2018.434	564.22 ± 1.57	58.76 ± 0.42	Stolker et al. (2020)
PDS 70 c	2016.3675	215.1 ± 7.0	285.01.5	Benisty et al. (2021)
PDS 70 c	2016.4167	254.1 ± 10.0	283.32.0	Benisty et al. (2021)
PDS 70 c	2018.1493	209.0 ± 13.0	281.20.5	Benisty et al. (2021)
PDS 70 c	2018.4671	235.5 ± 25.0	277.06.5	Benisty et al. (2021)
PDS 70 c	2019.1767	225.0 ± 8.0	279.90.5	Benisty et al. (2021)
PDS 70 c	2019.432	140.9 ± 2.2	280.4 ± 2.0	Wang et al. (2020)
β Pic b	2003.859	413 ± 22	34 ± 4	Nielsen et al. (2020)
β Pic b	2008.862	210 ± 27	211.49 ± 1.9	Nielsen et al. (2020)
β Pic b	2009.8151	299 ± 14	211 ± 3	Nielsen et al. (2020)
β Pic b	2009.922	339 ± 10	209.3 ± 1.8	Nielsen et al. (2020)
β Pic b	2009.922	323 ± 10	209.2 ± 1.7	Nielsen et al. (2020)
β Pic b	2009.9932	306 ± 9	212.1 ± 1.7	Nielsen et al. (2020)
β Pic b	2010.2726	346 ± 7	209.9 ± 1.2	Nielsen et al. (2020)
β Pic b	2010.7411	383 ± 11	210.3 ± 1.7	Nielsen et al. (2020)
β Pic b	2010.875	387 ± 8	212.4 ± 1.4	Nielsen et al. (2020)
β Pic b	2010.878	390 ± 13	212 ± 2	Nielsen et al. (2020)
β Pic b	2010.982	407 ± 5	212.8 ± 1.4	Nielsen et al. (2020)
β Pic b	2011.0863	408 ± 9	211.1 ± 1.5	Nielsen et al. (2020)
β Pic b	2011.2315	426 ± 13	210.1 ± 1.8	Nielsen et al. (2020)
β Pic b	2011.801	452 ± 3	211.6 ± 0.4	Nielsen et al. (2020)
β Pic b	2011.801	455 ± 5	211.9 ± 0.6	Nielsen et al. (2020)
β Pic b	2012.242	447 ± 3	210.8 ± 0.4	Nielsen et al. (2020)
β Pic b	2012.242	448 ± 5	211.8 ± 0.6	Nielsen et al. (2020)
β Pic b	2012.919	461 ± 14	211.9 ± 1.2	Nielsen et al. (2020)
β Pic b	2012.925	470 ± 10	212.0 ± 1.2	Nielsen et al. (2020)
β Pic b	2013.875	430.8 ± 1.5	212.43 ± 0.17	Nielsen et al. (2020)
β Pic b	2013.875	429.1 ± 1.0	212.58 ± 0.15	Nielsen et al. (2020)
β Pic b	2013.8808	430.2 ± 1.0	212.46 ± 0.15	Nielsen et al. (2020)
β Pic b	2013.941	425.5 ± 1.0	212.51 ± 0.15	Nielsen et al. (2020)
β Pic b	2013.941	424.4 ± 1.0	212.85 ± 0.15	Nielsen et al. (2020)
β Pic b	2013.944	425.3 ± 1.0	212.47 ± 0.16	Nielsen et al. (2020)
β Pic b	2014.853	356.2 ± 1.0	213.02 ± 0.19	Nielsen et al. (2020)
β Pic b	2014.936	350.51 ± 3.20	212.60 ± 0.66	Nielsen et al. (2020)
β Pic b	2015.0644	335.5 ± 0.9	212.88 ± 0.20	Nielsen et al. (2020)
β Pic b	2015.2507	317.3 ± 0.9	213.13 ± 0.20	Nielsen et al. (2020)
β Pic b	2015.341	332.42 ± 1.70	212.58 ± 0.35	Nielsen et al. (2020)
β Pic b	2015.749	262.02 ± 1.78	213.02 ± 0.48	Nielsen et al. (2020)
β Pic b	2015.848	250.5 ± 1.5	214.14 ± 0.34	Nielsen et al. (2020)
β Pic b	2015.914	242.05 ± 2.51	213.30 ± 0.74	Nielsen et al. (2020)
β Pic b	2015.927	240.2 ± 1.1	213.58 ± 0.34	Nielsen et al. (2020)
β Pic b	2015.974	234.5 ± 1.0	213.81 ± 0.30	Nielsen et al. (2020)
β Pic b	2015.985	234.84 ± 1.80	213.79 ± 0.51	Nielsen et al. (2020)
β Pic b	2016.0533	227.23 ± 1.55	213.15 ± 0.46	Nielsen et al. (2020)

Table 2
(Continued)

Object	Epoch	Sep (mas)	PA(°)	Reference
β Pic b	2016.056	222.6 ± 2.1	214.84 ± 0.44	Nielsen et al. (2020)
β Pic b	2016.234	203.66 ± 1.42	213.90 ± 0.46	Nielsen et al. (2020)
β Pic b	2016.291	197.49 ± 2.36	213.88 ± 0.83	Nielsen et al. (2020)
β Pic b	2016.709	142.36 ± 2.34	214.62 ± 1.10	Nielsen et al. (2020)
β Pic b	2016.7855	134.50 ± 2.46	215.50 ± 1.22	Nielsen et al. (2020)
β Pic b	2016.8811	127.12 ± 6.44	215.80 ± 3.37	Nielsen et al. (2020)
β Pic b	2018.711	140.46 ± 03.12	29.71 ± 1.67	Nielsen et al. (2020)
β Pic b	2018.7219	141.9 ± 5.3	28.16 ± 1.82	Nielsen et al. (2020)
β Pic b	2018.881	164.5 ± 1.8	28.64 ± 0.70	Nielsen et al. (2020)
HD 984 b	2019.514	233.8 ± 1.8	57.64 ± 0.29	Franson et al. (2022)
HD 984 b	2020.578	242.9 ± 1.7	51.61 ± 0.26	Franson et al. (2022)
HR 2562 b	2018.0836	669.44 ± 1.24	298.55 ± 0.2	Yimiao Zhang et al. (2023)
HR 2562 b	2018.2452	670.84 ± 2.83	298.74 ± 0.26	Yimiao Zhang et al. (2023)
HR 2562 b	2018.8836	685.76 ± 1.25	298.89 ± 0.13	Yimiao Zhang et al. (2023)

Note. The data from Benisty et al. (2021) includes astrometry points from Haffert et al. (2019), Mesa et al. (2019), and Wang et al. (2020). The data from Nielsen et al. (2020) includes astrometry points from Currie et al. (2011), Chauvin et al. (2012), Nielsen et al. (2014), and Lagrange et al. (2019).

Table 3
Radial Velocity Data Included

Object	Epoch	Relative RV (km s^{-1})	Reference
κ And b	2016.311	−1.4 ± 0.9	Wilcomb et al. (2020)
κ And b	2017.308	−1.4 ± 0.9	Wilcomb et al. (2020)
HD 1160 b	2017.843	7.343 ± 2.046	J. Beas Gonzalez; 2023, in preparation
HD 1160 b	2018.558	6.811 ± 2.670	J. Beas Gonzalez; 2023, in preparation
β Pic b	2013.9603	−15.4 ± 1.7	Snellen et al. (2014)
HR 8799c	2010.5356	−0.3 ± 2.1	Ruffio et al. (2019)
HR 8799c	2010.8425	0.5 ± 2.1	Ruffio et al. (2019)
HR 8799c	2011.5575	1.5 ± 2.4	Ruffio et al. (2019)
HR 8799c	2011.5603	0.7 ± 2.9	Ruffio et al. (2019)
HR 8799c	2011.563	0.5 ± 3.0	Ruffio et al. (2019)
HR 8799c	2013.5658	−4.3 ± 4.0	Ruffio et al. (2019)
HR 8799c	2017.8397	1 2	Ruffio et al. (2019)
HR 8799c	2020.5751	0.9 ± 2.4	Wang et al. (2021)
HR 7672 b	2020.4358	−6.074 ± 0.646	Ruffio et al. (2023)
HR 7672 b	2020.4385	−5.51 ± 0.58	Ruffio et al. (2023)
HR 7672 b	2020.7418	−6.899 ± 0.701	Ruffio et al. (2023)
HR 7672 b	2021.2644	−6.366 ± 0.368	Ruffio et al. (2023)
HD 4747 b	2020.7418	−5.107 ± 0.101	Xuan et al. (2022)

connected to the model parameters according to the following equations (e.g., Hilditch 2001; Ghez et al. 2003):

$$X = a(\cos E - e) \tag{3}$$

$$Y = a(\sqrt{1 - e^2} \sin E) \tag{4}$$

$$V_x = -\frac{\sin E}{1 - e \cos E}\sqrt{\frac{GM}{a}} \tag{5}$$

$$V_y = \frac{\sqrt{1 - e^2} \cos E}{1 - e \cos E}\sqrt{\frac{GM}{a}} \tag{6}$$

where G is the gravitational constant, E is the eccentric anomaly, e is the eccentricity, a is the semimajor axis, and M is the mass of the system. By transforming between measured observables and orbital observables, and then between orbital observables and model parameters, we can transform between measured observables and model parameters. This allows us to express a distribution that is uniform in the measured observables in terms of model parameters.

This fitting method reduces biases in orbital parameters by a factor of 2 in orbits with low phase coverage (O'Neil et al. 2019). For the eccentricity parameter, observable-based priors reduce the bias toward artificially high eccentricities usually found in fits with flat priors. Flat priors lead to a biased region in periastron passage (T_o) parameter space, where the T_o tends to artificially coincide with the observation epochs (Konopacky et al. 2016a). This bias is mitigated in observable-based priors because they suppress this biased region of the parameter space when sampling it. Thus, observable-based priors present a suitable fitting method for the orbital parameters of our object sample, which all have phase coverage <40%, and provide a different view on the eccentricity distribution of the companions when compared to the standard method for orbit fitting.

3.2. Recovering the Population Eccentricity Distribution

The individual eccentricity posterior distributions obtained with the observable-based prior method and the data described in the previous sections are presented on Figure 1. From these individual distributions, we now seek to determine the eccentricity distribution of the population. We adopt a Beta distribution for our underlying parent distribution for exoplanet eccentricity, similar to Hogg et al. (2010), Kipping (2013), Bowler et al. (2020), and Van Eylen et al. (2019). The Beta distribution is a convenient choice for this study because its values, like the eccentricities, range from 0–1. It also only requires two positive parameters, α and β, which allow it to present a variety of shapes, such as linear, Gaussian, and uniform. The Beta distribution is represented by:

$$f(e, \alpha, \beta) = \frac{\Gamma(\alpha + \beta)e^{\alpha - 1}(1 - e)^{\beta - 1}}{\Gamma(\alpha)\Gamma(\beta)}. \tag{7}$$

Here, Γ is the Gamma function. We use the posteriors in our sample and the beta function fitter present on the SciPy package (Virtanen et al. 2020), which uses the MLE method, for fitting our posteriors to the distribution. We perform our fitting using a bootstrapping method by repeating the following
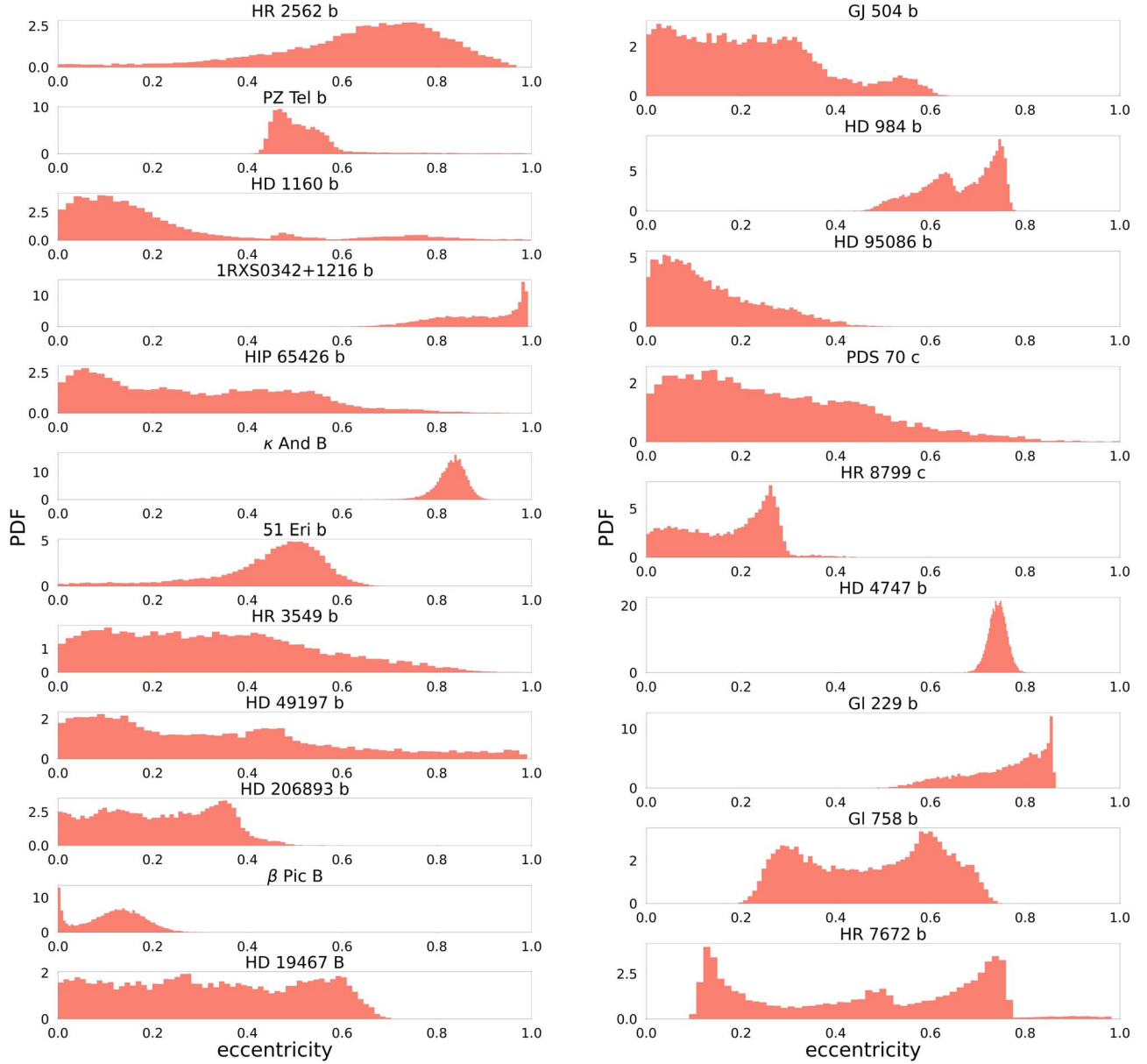
Figure 1. The weighted eccentricity distribution derived via our orbital fits for the sample of 21 companions using observable-based priors. The *x*-axis represents the eccentricity values, and the *y*-axis represents the normalized incidence of eccentricities. Here, the fits include both astrometric and RV data points.

steps: (1) sampling an eccentricity point from each posterior chain, and then (2) fitting a Beta distribution to those points using the SciPy Beta fitting functionality.

3.3. Beta Distribution Recovery Simulation

In order to validate the choice of using the MLE fitter for obtaining our estimated α and β distributions, we develop a procedure similar to the recovery analysis presented in Bowler et al. (2020). The purpose of this exercise is to test our bootstrapping method. We obtain points from the $\alpha = 0.867$, $\beta = 3.03$ distribution presented by Kipping (2013) for warm Jupiters and points from the $\alpha = 0.95$, $\beta = 1.30$ distribution presented by Bowler et al. (2020). We vary the number of points taken, taking N = 10, 20, 50, and 100. "N" represents the number of companions that contribute to our fitting sample. Our resulting recovered distributions are presented in Tables 4

Table 4
Beta Distribution Shape Parameters (Kipping)

N	α	β
10	$1.00^{+0.60}_{-0.32}$	$3.65^{+2.70}_{-1.37}$
20	$0.93^{+0.34}_{-0.22}$	$3.31^{+1.46}_{-0.93}$
50	$0.89^{+0.18}_{-0.14}$	$3.13^{+0.79}_{-0.58}$
100	$0.88^{+0.12}_{-0.10}$	$3.08^{+0.51}_{-0.42}$

Note. The original input distribution parameters are $\alpha = 0.867$, $\beta = 3.03$.

(Kipping) and 5 (Bowler). In the plots with Beta distribution probability density functions (PDFs; Figure 2), we plot the "true" input distribution in a darker blue/red shade along with 100 randomly sampled distributions from within the confidence intervals in a lighter blue/red shade.
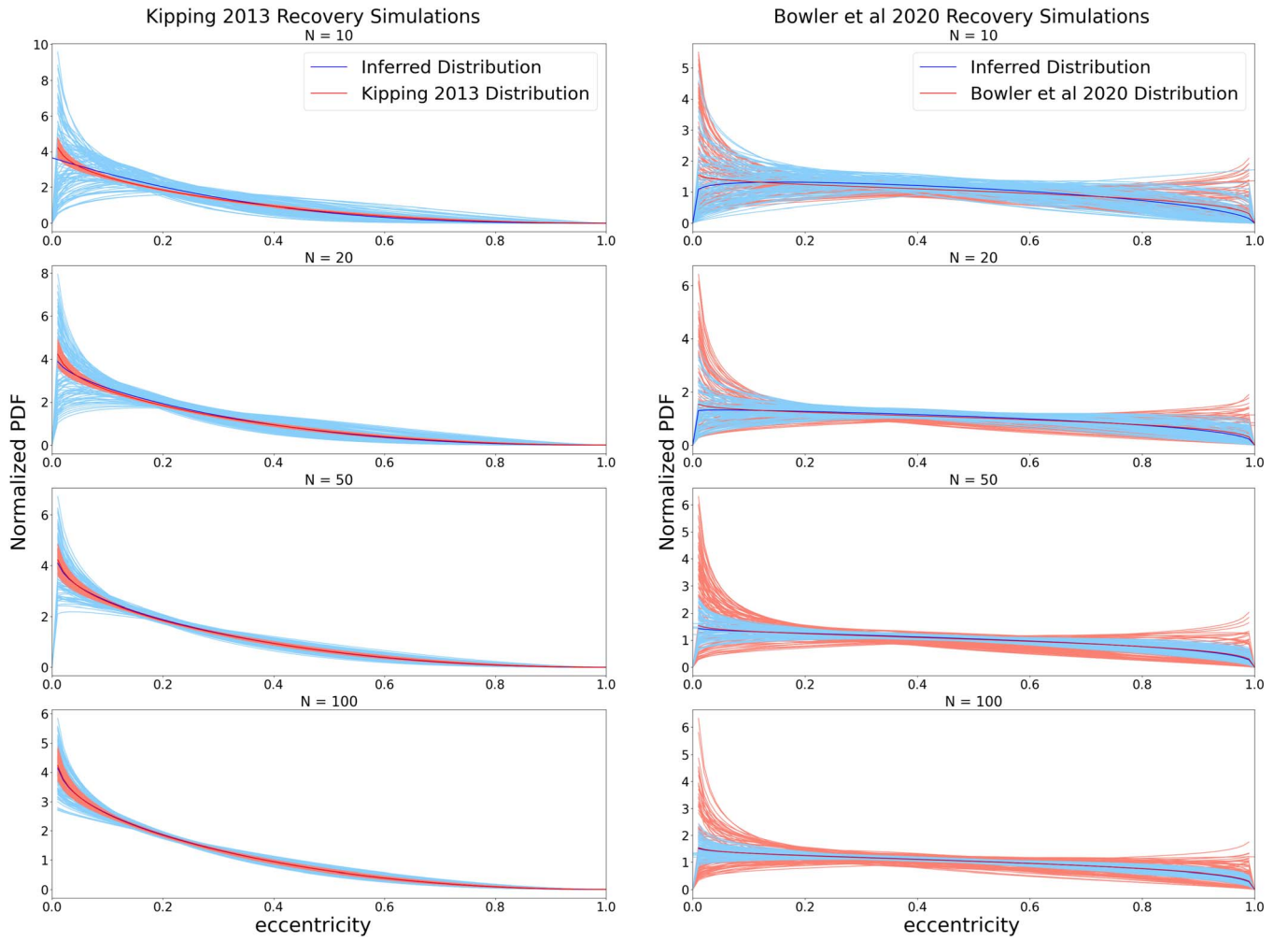
Figure 2. The resulting distributions of our recovery simulations plotted on top of the distributions from where the synthetic data is drawn for Kipping (2013) (a) and Bowler et al. (2020) (b). The original distributions are represented in red, and the obtained recovered distributions are presented in blue. The different columns are labeled with the distributions obtained for differing N values (i.e., number of planets in the sample, or number of points drawn from the true input distribution). The shaded regions represented in lighter blue and red represent the possible distributions encompassed by our confidence intervals. The purpose of this exercise is to validate our bootstrapping technique and check that we get matching results from the original input (or true) distributions.

Table 5
Beta Distribution Shape Parameters (Bowler)

N	α	β
10	$1.10^{+0.69}_{-0.37}$	$1.53^{+1.02}_{-0.54}$
20	$1.02^{+0.38}_{-0.25}$	$1.40^{+0.56}_{-0.36}$
50	$0.98^{+0.21}_{-0.16}$	$1.34^{+0.30}_{-0.23}$
100	$0.96^{+0.14}_{-0.11}$	$1.32^{+0.20}_{-0.16}$

Note. The original input distribution parameters are $\alpha = 0.95$, $\beta = 1.30$.

4. Results

In this section, we show our results for the eccentricity distributions of individual objects and different populations of directly imaged companions. We find that some objects presented significant eccentricity shifts when using observable-based priors instead of uniform priors (Section 4.1.2). For our full sample of 21 objects, we obtain shape parameters $\alpha = 1.09^{+0.30}_{-0.22}$ and $\beta = 1.42^{+0.33}_{-0.25}$ (Section 4.1.1). We test whether leaving one object out of the sample changes our results (Section 4.1.3), and find that our sample does not have

any true outliers. We also test splitting the sample by companion mass (low and high), and find that the consistency between the distributions changes depending on where intermediate-mass objects are placed (Section 4.1.4). Finally, we simulate how much orbital coverage is needed to obtain reliable posteriors in our distributions, both for uniform and observable priors (Section 4.2). We obtain 15% of the period of the orbit as a result.

4.1. Eccentricity Distributions

4.1.1. Population Eccentricity Distribution

We use the posteriors from 21 companions to investigate changes in the inferred eccentricity of individual systems due to observable-based priors, as well as to obtain an inferred eccentricity parent distribution. Following the procedure from Section 3.3, we randomly sample the posteriors to obtain a possible range of α and β shape parameters of the parent Beta distribution.

Our result for the eccentricity distribution of the entire sample is presented in Figure 3. We obtain a beta distribution with $\alpha = 1.09^{+0.30}_{-0.22}$ and $\beta = 1.42^{+0.33}_{-0.25}$. This shape presents a
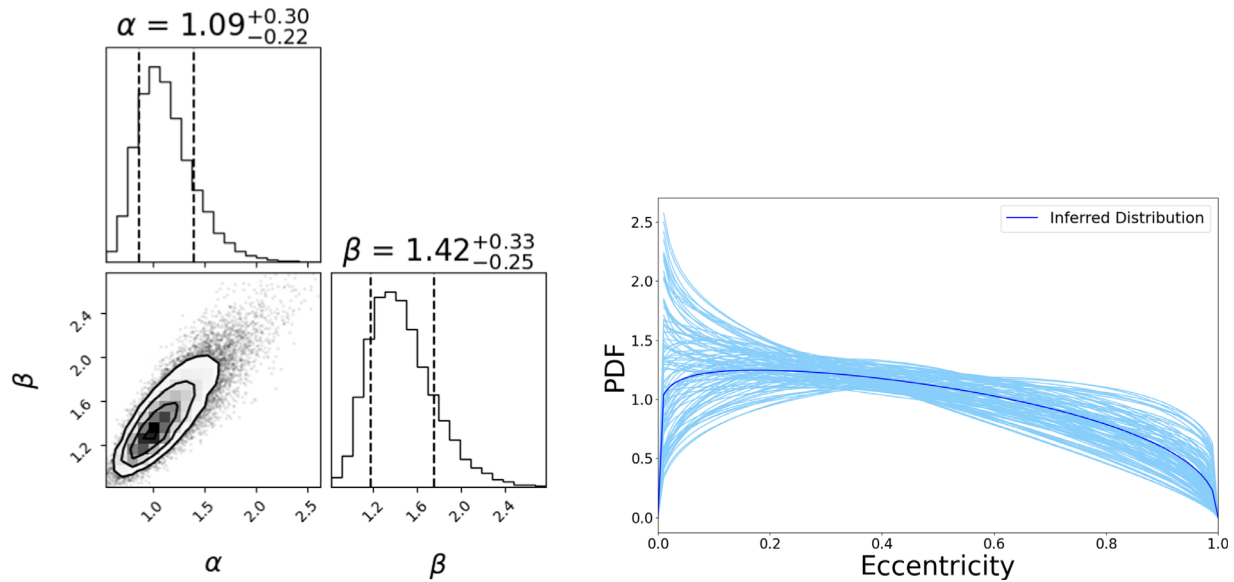
Figure 3. Inferred distribution for the sample of directly imaged companions. The beta fit results (68th percentile) from sampling the posteriors are presented in panel (a). The distribution (dark blue) is then plotted (panel (b)) with 100 distributions (light blue) that encompass our uncertainties. The lighter curves indicate the possible ranges of α and β from the fitting distribution.

near-uniform distribution for the eccentricities of substellar companions, with a slight tendency toward lower eccentricities.

In order to determine if two derived population distributions are consistent with each other, we estimate the consistency of their respective parameters α and β. The procedure defined here is a general method, which we use to determine consistency of two Beta probability distributions throughout this work. We define two random variables as the differences $\delta\alpha = \alpha_2 - \alpha_1$ and $\delta\beta = \beta_2 - \beta_1$ where α_1, β_1 defines the first population, and α_2, β_2 defines the second population. If the two populations are consistent, the distributions of both $\delta\alpha$ and $\delta\beta$ should be consistent with zero. The distributions of $\delta\alpha$ and $\delta\beta$ are calculated by sampling the respective distributions of α_1, α_2, β_1, and β_2 in a bootstrapping manner from the resulting fits (i.e., sampling the α_1, β_1 and α_2, β_2 pairs from the fit chains), and calculating their differences at every iteration. We then calculate the p-value of the sample:

$$\mathcal{P} = p_{\text{value}} \tag{8}$$

by integrating the 2D distribution of $(\delta\alpha, \delta\beta)$ inside the contour of constant density that goes through the origin. The integration is performed using a Gaussian kernel density estimator. An example of this process along with more details on how $\mathcal{P}$ is calculated is shown in Appendix B.

We alternatively calculate $\mathcal{P}$ using the Kolmogorov–Smirnov (K-S) test using in the package ndtest in Python (github.com/syrte/ndtest). For this test, the discrete values of x and y for the PDF must be used, so we sample 100 pairs of α and β from the chains of two distributions, obtain 1 value from each of the pairs, and compare the two using the K-S test. We obtain fully consistent results between the kernel density estimate and the K-S test, and thus report $\mathcal{P}$ from the kernel density herein.

For the distributions presented in Bowler et al. (2020) and Kipping (2013), we do not have the posterior chains of α and β pairs so we randomly sample from uniform distributions with the α and β ranges (including the uncertainties) given by these works. When comparing our Beta distribution to the
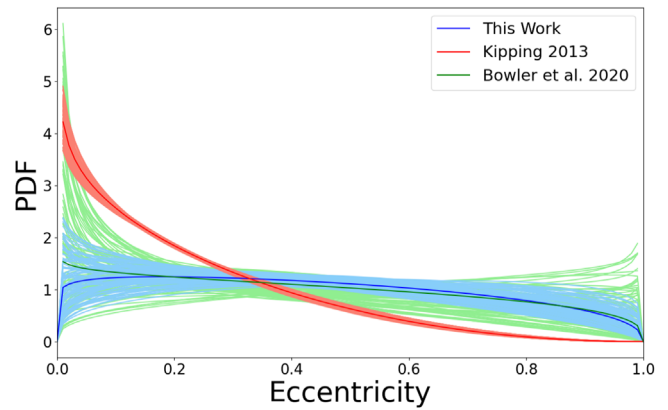
Figure 4. Comparison of the obtained beta distribution for the entire sample with the distributions of Bowler et al. (2020) and Kipping (2013). We note that the distribution obtained by Kipping (2013) is for short-period warm Jupiters, whereas Bowler et al.'s (2020) distribution is for long-period extrasolar planets and brown dwarfs. Our sample closely resembles that used by the latter's work, but with a lower high-eccentricity incidence—likely due to the change from uniform to observable priors.

distributions found by Bowler et al. (2020) and Kipping (2013), we find that our distribution is consistent with Bowler et al.'s (2020; $\mathcal{P}$ of 0.77) but not with Kipping's (2013; $\mathcal{P}$ of 0.000; see Figure 4).

The reasons for the inconsistency with Kipping (2013) could involve the fact that Kipping's (2013) distribution is for short-period exoplanets (therefore not including the long-period objects that populate our sample), the lower N in our sample (21 versus 396 objects), and the difference in detection method for the objects. Kipping's (2013) sample used RVs as the primary detection method of the companions, while we used direct imaging. Kipping (2013) also has much smaller confidence intervals than both our shape parameters and Bowler et al.'s (2020) shape parameters. This, again, is likely due to a small confidence interval in the individual eccentricities as well as the limited sample size (<10%) of the direct imaging sample when compared to the RV sample.

As mentioned in Section 3.1, the traditional prior framework often presents a bias toward higher eccentricities. This is why, when comparing our distribution to the one obtained by Bowler et al. (2020), we note that our parent distribution presents a reduced curved peak near high eccentricities, favoring slightly lower eccentricities. This could indicate that the bias toward higher eccentricities in individual orbits can also provide a bias toward higher eccentricities in the underlying parent distribution, particularly when the sample size is small. The observable-based prior aims to avoid such a bias in individual orbit fits; however, it is not completely capable of eliminating it. We also note that our low-eccentricity end presents a smaller peak (near $e = 0$), likely due to the fact that we did not include more than one planet from multiplanet systems (e.g., HR 8799 b,d, and e are not included) into our sample. Including those objects could cause an artificial increase in the PDF at low eccentricities since their eccentricities are correlated by being in the same system and being stable.

4.1.2. Individual Objects with Significant Eccentricity Shifts

Some objects present a significant shift in their eccentricity distributions when comparing orbit fits from uniform priors and observable-based priors. The orbits with significant eccentricity shifts in our sample are HD 49197 b, HR 2562 b, HIP 65426 b, HD 1160 b, and PZ Tel b. These five objects compose more than 20% of our companion sample.

HD 49197 b had its eccentricity posterior change from $0.62^{+0.33}_{-0.43}$ to $0.28^{+0.29}_{-0.20}$, (weighted median of the posterior distribution, 50th percentile), with the uncertainties encompassing the 68th percentile values, favoring lower-eccentricity solutions when fit with observable-based priors. HR 2562 b had its eccentricity posterior change from $0.49^{+0.44}_{-0.36}$ to $0.66^{+0.16}_{-0.33}$, changing from a bimodal distribution with eccentricity modes at ≈0.2 and 0.9 to a fit that spans a large amount of eccentricity values but disfavors eccentricities > 0.9. HIP 65426 b had its posteriors change from $0.57^{+0.29}_{-0.38}$ to $0.26^{+0.41}_{-0.20}$, favoring lower-eccentricity values with the observable-prior fit.

One object that is of particular interest is HD 1160 b, one of two known companions orbiting HD 1160. When fitting the orbit of HD 1160 b using uniform priors, there is a strong preference for higher eccentricities ($\geqslant0.9$; see Figure 14). With observable-based priors, however, the eccentricity distribution strongly shifts toward lower values. We validate the lower-eccentricity solution in two ways: (1) by checking consistency with an updated orbital fit that incorporates the two new RV measurements reported in Section 2.2, and (2) by assessing the stability of the system, given its age. As discussed below, both approaches validate the lower-eccentricity solution, indicating that the observable-based prior, in this case, is doing exactly what it was designed to do: minimize the biases in the posteriors when in the prior-dominated regime.

1. We fit HD 1160 b's orbit using uniform priors with orbitize!. The main difference from the previous fit is that we include two RV data points, presented in Section 2.2. The addition of two RV data points was sufficient to shift the eccentricity distribution, yielding the distribution presented in Figure 15. This distribution resembles the observable-based priors distribution (even without RVs) much more closely (see Figure 5).

2. To analyze whether the system would allow for such a high eccentricity for one of the companions, we ran
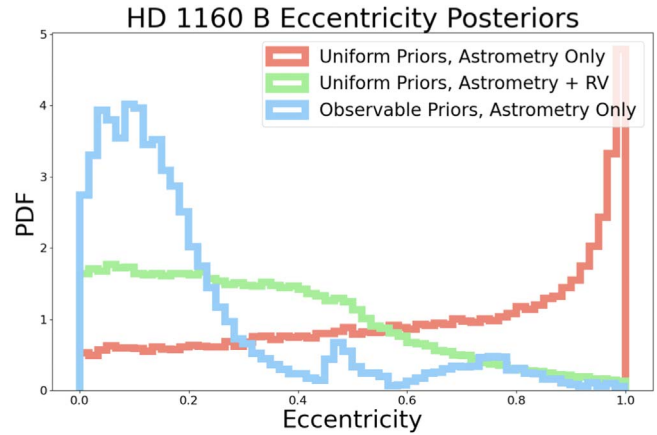

Figure 5. Comparison of the eccentricity posteriors for three different prior + data configurations of HD 1160 b.

stability simulations for the age of the system. Using the WHFast integrator on REBOUND (Rein & Tamayo 2015), we integrate the system for 120 Myr, which is the oldest estimate for the system's age given by Garcia et al. (2017). We assess stability using the mean exponential growth of nearby orbits (MEGNO; Cincotta et al. 2003). Orbits that present an MEGNO $\leqslant 2$ over a period of time are considered stable. We keep their masses fixed to their best-fit values of 0.1 $M_{\odot}$ (J. Beas Gonzalez et al 2023, in preparation) for HD 1160 b and 0.22 $M_{\odot}$ (Nielsen et al. 2012) for HD 1160 C. We use the orbital posteriors for both HD 1160 b and HD 1160c from orbitize! to assess the stability of the system. We bin the b and c posteriors into 10 bins, with each bin spanning a 0.1 spacing in eccentricity (e.g., $0.1 < e_b < 0.2$, $0.3 < e_c < 0.4$). For each bin, we draw 1000 random orbit combinations from the posteriors and assess whether they remain stable for the age of the system. This yields 100,000 possible orbit combinations from the objects' posteriors, with 1000 per bin (and a total of 100 bins). We then assess how many orbits in each bin remain stable using the MEGNO parameter. We do this for two different posteriors for HD 1160: with and without the RVs.

We present a contour plot of the 100,000 possible orbit combinations of HD 1160 b and c, with the contours representing what percent of the random draws remained stable for the age of the system. The contour is shown in Figure 6. The figure illustrates that HD 1160 b is unlikely to have eccentricity values > 0.9, which was a value favored by the uniform prior fit without RV measurements. When we test this simulation set with HD 1160 b's orbital posteriors without RVs, we obtain an equivalent plot, showing that the majority of solutions for HD 1160 b and c disfavor very eccentric orbits for both objects.

For PZ Tel b, a new astrometry point was sufficient to also change the eccentricity distribution of the object. The 2018 epoch added to our fits is shown in Table 2. Prior to 2018, works that presented orbit fits for this object indicated that it had a very high eccentricity (e.g.,Ginski et al. 2014; Maire et al. 2016; Beust et al. 2016). The new astrometry point for PZ Tel b, obtained in 2018, changes the orbital period coverage of the companion from $3.9^{+1.9}_{-1.3}$ % to $6.2^{+2.9}_{-2.1}$ %, calculated from the
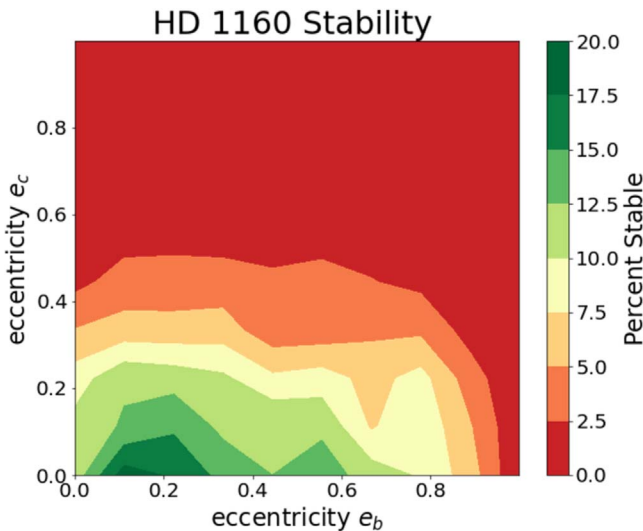
Figure 6. Stability contour for the HD 1160 system obtained by binning the companions' posteriors in eccentricity bins of 0.1 width. The colors represent the percent of the 1000 random draws for each bin that remain stable for the age of the system. HD 1160 b and c orbits are shown to disfavor very eccentric orbits by the stability constraint.

Figure 7. Eccentricity posteriors of PZ Tel B with (red) and without (blue) the 2018 epoch.

weighted median of the posterior distribution (50th percentile), with the uncertainties encompassing the 68th percentile of our orbit fits for the period and the current astrometric coverage increase from 7 to 11 yr. This new point's impact on the distribution implies that there could be a minimal orbital period coverage needed in order to obtain eccentricity posteriors that are meaningful for directly imaged planets. Our posteriors obtained with observable-based priors with and without the 2018 epoch are presented in Figure 7.

4.1.3. Leave-one-out Cross Validation

Given the small sample size of directly imaged companions, there is a possibility that a single object with a narrow eccentricity posterior may noticeably impact the resulting population distribution. To test for this, we analyze the impact of removing one single object from the sample for each of the 21 objects. We do that by re-running the beta distribution fit on the entire sample, but excluding one object at a time. We characterize a large impact as a change in expected α and β parameters for the underlying distribution of eccentricity that falls outside of the 1σ confidence level on the procedure described in in Section 4.1.1.

We find that removing any single object from our population does not yield $\delta\alpha$ and $\delta\beta$ to be outside of the 68% confidence interval using $\mathcal{P}$ defined in Section 4.1.2. We therefore conclude that our sample does not have obvious outliers. The object that produces the most different distribution is 1RXS0342+1216 b, which is a high-mass companion with eccentricity of $0.94^{+0.04}_{-0.11}$ (given from our orbit fit's 68th percentile, with the central value being the weighted median of the posteriors). Even in this case, we estimate that the two distributions have parameters that are consistent with a $\mathcal{P}$ of 0.50.

4.1.4. Separating the Sample by Companion Mass

We also separate the sample in two populations based on the mass of the companion. The goal is to identify any possible
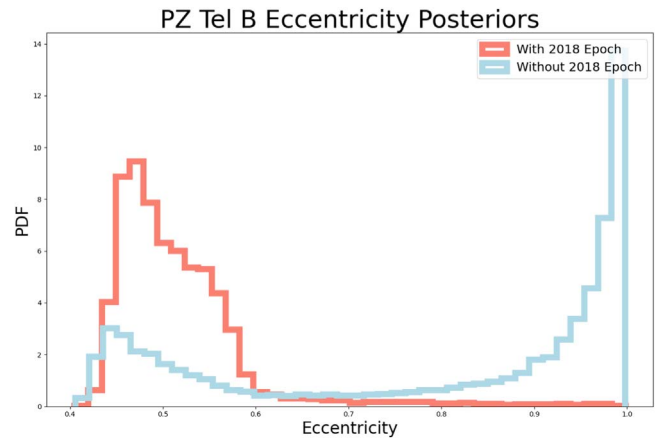
differences in the eccentricity as a function of mass. Such a distinction could be correlated with the masses expected for gas giant planets (companions with mass $\leqslant 15$ M_J) and brown dwarf companions (companions with mass > 15 M_J). If differences in eccentricity distributions are found between the populations, eccentricities can potentially be used to constrain formation mechanisms. The complexity here is the use of a mass boundary for distinguishing between populations. If the definition of a planet versus a brown dwarf is related to formation, it is unlikely that 15 M_J is a meaningful boundary (e.g., Bodenheimer et al. 2013; Mordasini et al. 2012). Additionally, most of the masses assumed for these companions are from evolutionary models and rely on uncertain properties such as system age (e.g., Carson et al. 2013; Hinkley et al. 2013). Even with these caveats, it is still beneficial to look for differences between more- and less-massive companions in the context of distinction between these populations.

When classifying these objects into the low-mass and high-mass categories, the intermediate-mass objects at the boundary, namely β Pic b, HR 2562 b, and κ And b, could have a strong impact on the final result. Thus, we re-run our "planet" versus "brown dwarf" population placing them in either of the populations to analyze whether the eccentricity distribution of each population changes. The mass estimates are plotted against the eccentricity estimates (68th percentile) in Figure 8. The mass estimates and respective references are shown in Table 1.

Including all of the boundary objects in the planet sample makes it composed of nine companions. When none of them are in the sample, the planet population comprises only six objects. This low sample size can cause an outlier to significantly skew the eccentricity of the entire population.

When switching β Pic b from the planet to brown dwarf population, we find no significant change in our $\mathcal{P}$ values that measure the consistency between the two populations. This is not the case for κ And b and HR 2562 b, in particular the former. Table 6 represents our consistency parameter (defined as the $\mathcal{P}$ value) for different combinations of these objects' classifications. κ And b, when considered a brown dwarf, produces distributions of planets and brown dwarfs that are different from each other. We illustrate two of these extreme cases (highest $\mathcal{P}$ and lowest $\mathcal{P}$) in Figure 9. The "extreme" cases yield, respectively, planet population parameters of $\alpha = 1.04^{+0.41}_{-0.28}$ and $\beta = 1.82^{+0.58}_{-0.42}$ versus $\alpha = 1.59^{+1.26}_{-0.60}$ and
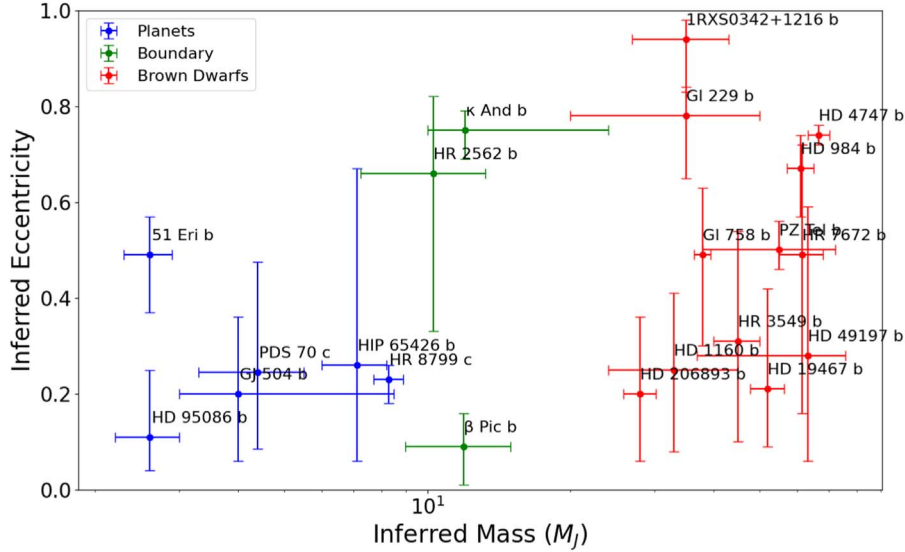
Figure 8. The mass of the companions plotted against the eccentricity of the companions. Mass estimates are from the literature, while eccentricity estimates are from this work. Error bars on the eccentricity represent the 68th percentile of the orbital fit. The blue dots represent "planets," or objects under 15 M_J, while red dots represent "brown dwarfs," or objects with masses above 15 M_J. Green dots are "boundary" objects: intermediate-mass objects that could be in either distribution.

Table 6
Consistency between Planets versus Brown Dwarfs Distributions Represented as $\mathcal{P}$ (P-value)

	κ And b (Planet)	κ And b (Brown Dwarf)
HR 2562 b (Planet)	0.373	0.001
HR 2562 b (Brown Dwarf)	0.139	0.000

Note. Impact of the classification of intermediate-mass objects on the consistency between the planet and brown dwarf populations. The consistency is measured as $\mathcal{P}$ measuring the similarity of the estimated parameters α and β that define the Beta distribution. A $\mathcal{P} > 0.68$ would mean that the two distributions are consistent, while <0.01 means that the two distribution are likely different. For this table, β Pic b is considered a planet, although considering it a brown dwarf produces no significant changes in $\mathcal{P}$.

$\beta = 5.03^{+3.73}_{-2.01}$. Their brown dwarf distributions are parameterized by $\alpha = 1.33^{+0.64}_{-0.39}$ and $\beta = 1.39^{+0.54}_{-0.34}$ versus $\alpha = 1.41^{+0.62}_{-0.40}$ and $\beta = 1.31^{+0.43}_{-0.29}$. It is clear from Figure 9 and Table 6 that a small portion of objects can shift whether the two populations have similar distributions or not. This is likely due to the small sample size both for the entire population but especially for the subsamples separating high- and low-mass objects.

We also test the mass separation distributions completely omitting the three boundary objects, and find planet and brown dwarf populations that are similar to Figure 9 (bottom panel). However, the low sample size of the population (only six planets, none of which have eccentricities above ≈0.7 in their posteriors' 68th percentile) is significantly affected by a single object with higher eccentricity, such that our population distribution derivation is prone to higher uncertainties and to being skewed by any outliers in the sample. Given these results and the uncertainties and caveats around masses, we conclude that our current sample and its components' individual eccentricity distributions do not provide enough constraints to affirm that different formation pathways are underway for substellar companions above and below ∼15 M_{Jup}.

4.1.5. Separating the Sample by Companion Separation

We also test splitting our companion sample by separation from the host star. The interest in performing this comparison comes from the possible distinction between core accretion and gravitational instability companions, since gravitational instability models tend to favor formation farther away from the host star (e.g., Mayer et al. 2004), while core/pebble accretion companions are most efficiently formed closer to the host star (e.g., Dodson-Robinson et al. 2009). The 68th percentile eccentricity posteriors are plotted against the separation of the companions, in astronomical unit, in Figure 10.

We also test splitting the population into "close" and "wide" separation companions, with the cutoff of 30 au. This cutoff allows the companion sample to be split approximately in half between the 5–30 au and 30–100 au bins. It is also close to the 35 au threshold set by Dodson-Robinson et al. (2009), beyond which the critical mass obtained by core accretion objects cannot occur and where gravitational instability becomes a more efficient companion formation mechanism. We find that the two populations are consistent with each other, with a $\mathcal{P}$ of 0.85. Their distributions are shown in Figure 11.

4.2. Minimal Orbital Coverage Simulations

Given the major shift in the eccentricity distribution of PZ Tel b given the addition of new data (Section 4.1.2), we simulate how much orbital period coverage we need in order to obtain a meaningful posterior distribution for eccentricity. The main goal of this analysis is to stipulate whether we can obtain meaningful results on these objects with the currently available astrometry. For context given the sample we have been exploring, we examine the best estimate for the orbital coverage as a fraction of the period (in percent), plotted against the best estimate for the eccentricity of each source, with error bars encompassing the possible values presented in each individual eccentricity distribution. We obtain the orbital coverage by dividing the current astrometric coverage for each
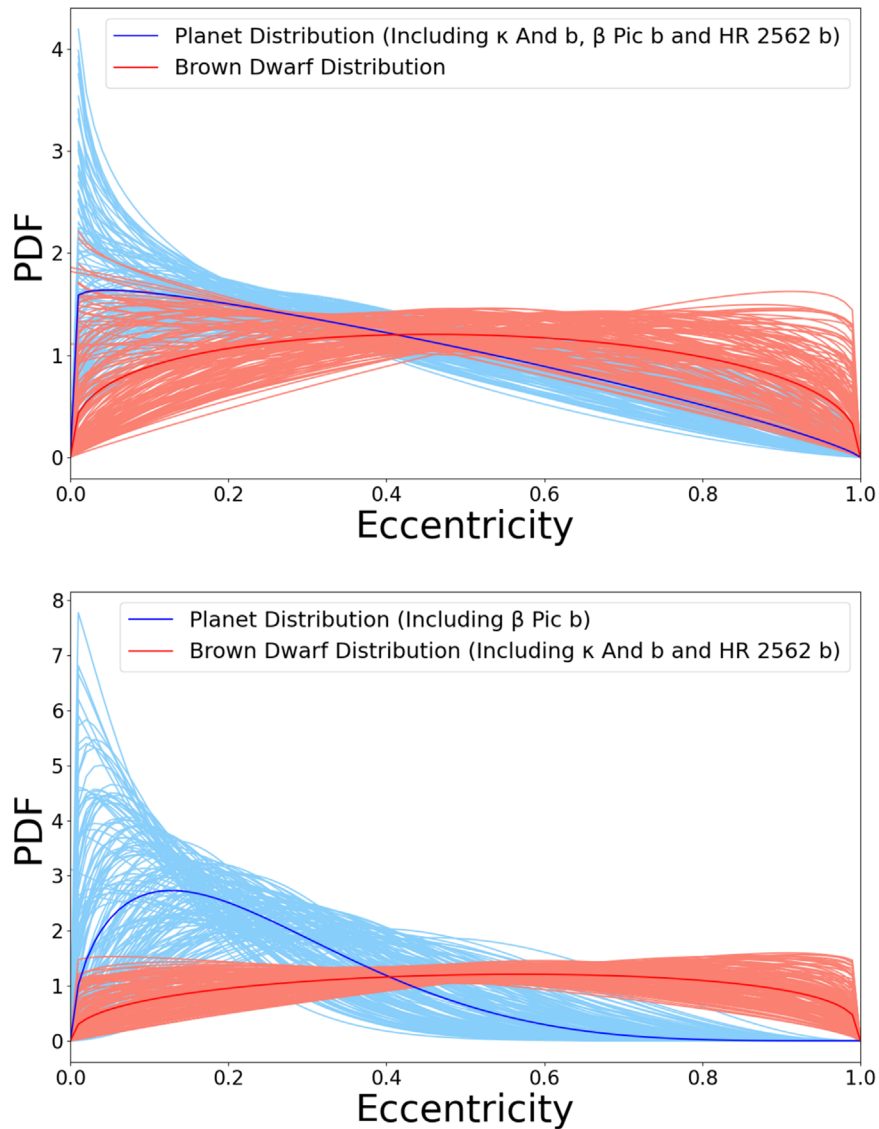
Figure 9. Comparison of "planet" vs. "brown dwarf" distributions for different combinations of intermediate-mass objects: for our highest $\mathcal{P}$ case (i.e., most similar distributions) and lowest $\mathcal{P}$ case (i.e., most different distributions).

object by its inferred orbital period. The results are presented in Figure 12. The average orbital period coverage for the sources in our sample is 7.4%, calculated from weighted median values of our sample's orbital period fits and the astrometric coverage, in years, for each object in the sample.

In order to assess the minimum required orbital phase coverage, we simulate data to indicate how an object's orbital configuration affects the amount of coverage needed to obtain reliable posteriors. We perform this simulation with the hope of finding a trend for how much information must be obtained for each system such that a meaningful posterior can be extracted —and, in turn, a meaningful eccentricity underlying parent distribution can be obtained.

First, we simulated orbits with properties that are representative of the average object in our sample. We define a period of 200 years, and inclination of 60 degrees and periastron passage occurring in 2150. The total system mass is fixed at 0.68 M$\odot$. We vary the eccentricity of a given orbit to see how its value affects the posteriors for a given orbital period coverage. We calculate astrometry points based on these orbital parameters, starting in the year 2021. We generate astrometry

points in order to simulate increasing orbital phase coverage. The astrometry "time step" represents 1% of the period of the orbit. The astrometry encompasses uncertainties on the order of milliarcsecond precision, as is typical for high contrast imaging instruments (Konopacky et al. 2014). To simulate instrument differences and other systematic factors, the simulated astrometry points also have noise randomly sampled from a Gaussian distribution centered at 0 and with the width of the astrometric uncertainty. This simulated astrometry is used to run orbit fits analogous to those in the rest of our analysis. We run our observable-based prior and uniform prior orbit fitter 100 times for each orbital eccentricity value, increasing the astrometry and hence the phase coverage with each successive run. In order to consider a simulation "successful," the real input eccentricity, To, inclination and period must be within the 68% confidence interval given by the fit.

We find that the orbital coverage of 15% was the minimum value needed to obtain 68 successful posteriors (out of 100 trials) for all eccentricity value variations, both for observable and uniform priors. This encompasses 30 yr of observations from 2021–2051 for this specific orbit. The orbital coverage
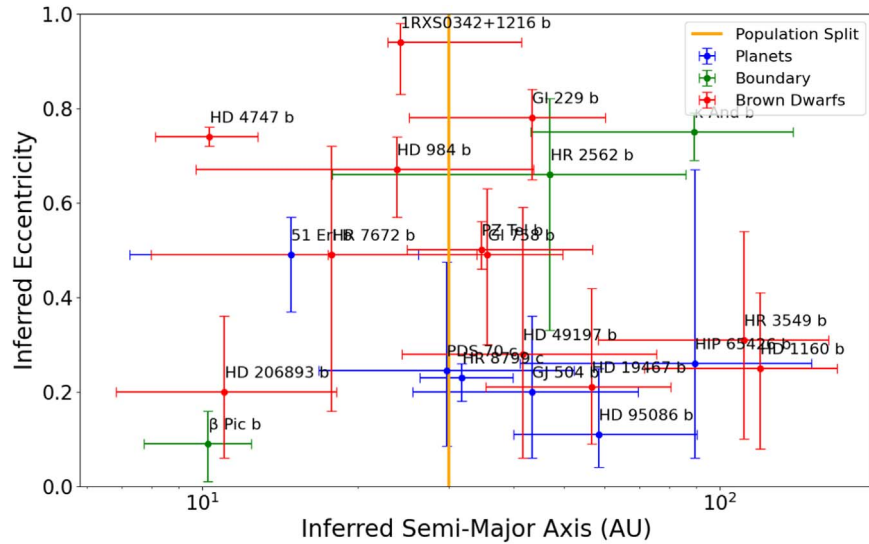
Figure 10. The semimajor axis plotted against the eccentricity of the companions. Semimajor axis values are calculated from the 68th percentile of our orbital fits. Error bars on the eccentricity represent the 68th percentile of the orbital fit. The blue dots represent "planets," or objects under 15 M_J, while red dots represent "brown dwarfs," or objects with masses above 15 M_J. Green dots are "boundary" objects: intermediate-mass objects that could be in either distribution. In orange, we plot the separation cutoff where we split our sample between "Close" and "Wide" separations.
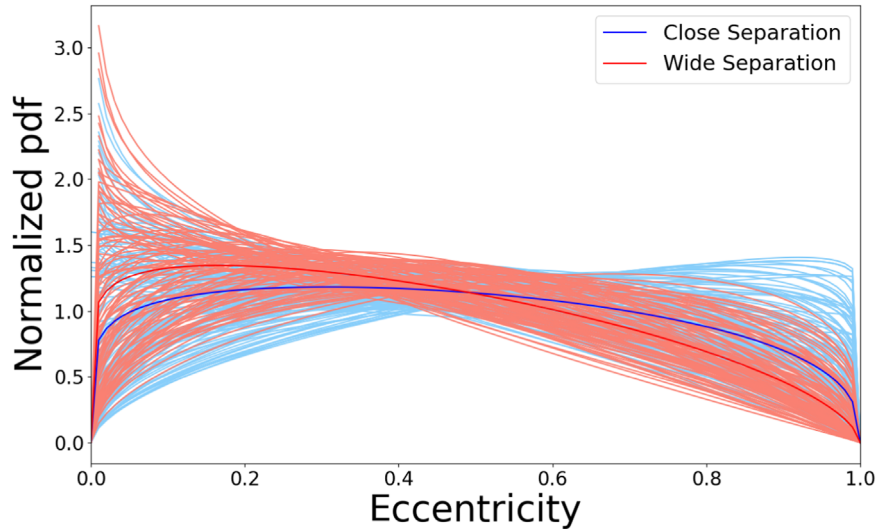
Figure 11. The "close" vs. "wide" separation companion populations, with the split happening at 30 au. The two distributions are consistent with each other, with a $\mathcal{P}$ of 0.85.

value is defined differently from the Lucy (2014) 40% minimum orbital phase coverage, since here it is based off of the period of the orbit and not the orbital arc. Thus, the 15% period coverage is dependent on an orbital arc where the planet does not go through periastron passage during observation, which should be the case for the majority of directly imaged planets, as the planet spends the least amount of time of its orbit at periastron. The phase coverage obtained by this specific orbit spans ≈3%–15% of the orbit's phase (depending on eccentricity, which was varied in the interval from 0.1–0.9 in steps of 0.1), which is less than the value obtained by Lucy (2014). Another difference is that in Lucy (2014), the total system mass was a free parameter in the fit, while for our case (as is standard for most direct imaging orbit fits), the mass was kept fixed. Having the total system mass as a free parameter is likely a reason as to why Lucy's (2014) phase coverage requirement is larger than those obtained with our simulations. We also test the needed orbital coverage for 100 yr and 400 yr period orbits

and find no dependence on period as long as the orbital period coverage remains the same (at least 15% of the period). Note that this is a rule of thumb only—some orbits may require more coverage than this, while others may require less. The 15% coverage number found here represents a minimum point at which the orbit posteriors for directly imaged planets should realistically be used to derive population distributions. Our results are presented in Figure 13.

For the median period of objects in our sample (≈251 yr), we would need 38 yr of data to begin to have reliable posteriors. Looking at specific example cases, HD 19467 B has an estimated period of $426.14^{+115.89}_{-98.13}$ yr (weighted median of the fit, with uncertainties spanning the 68th percentile of orbital fit) but our astrometry only covers 7 yr (or $1.6^{+0.5}_{-0.4}\%$), calculated from the 68th percentile of the fit, of the estimated orbital period—which means that our parameter posteriors for this object may not be reliable. This result is also exemplified in
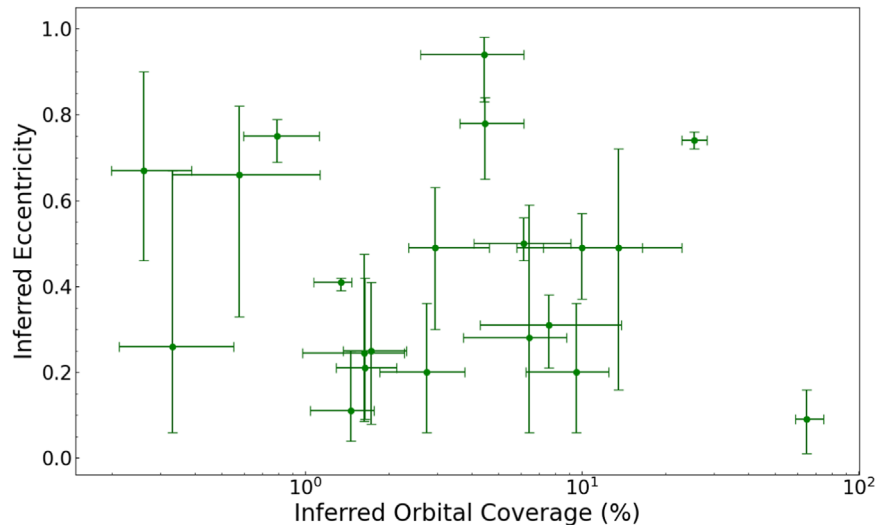
Figure 12. The inferred orbital coverage of each object in the sample, calculated as a fraction of the astrometric coverage and the period fit, plotted against the eccentricity of the object. This is from the real data used in our sample. Most of the sources have less than 10% orbital period coverage, with four objects presenting less than 1% period coverage.

Section 4.1.2, where PZ Tel b's orbital coverage increase from $3.9^{+1.9}_{-1.3}$ completely shifted the eccentricity distribution of the companion. However, given that we still have less than 15% coverage for PZ Tel b, we might expect additional changes in the posteriors as more data is collected.

5. Discussion

In this work, we use observable-based priors to fit for the orbital parameters of 21 directly imaged substellar companions with updated astrometry and RV measurements from the literature. Revisiting the analysis done by Bowler et al. (2020) with a different set of priors, the goal is to obtain the eccentricity distribution of the entire population and analyze if there is any difference in the eccentricity distributions of planet and brown dwarf populations. Differences in these populations' eccentricity distributions could potentially be signs of different formation mechanisms: with planets mainly forming from protoplanetary disks and thus presenting low eccentricities, and brown dwarfs forming similarly to binary star systems (for instance, via disk fragmentation) and therefore spanning all values of eccentricities (Bowler et al. 2020).

5.1. Choice of Priors

The vast majority of exoplanets and brown dwarfs in our directly imaged population have long periods, due to their fairly large distance from the host star. Consequently, their orbital arcs covered by current astrometry span a small fraction of their orbital periods, yielding orbital fits that are severely undersampled. Such undersampling of data can cause all results of orbit fitting to be in a prior-dominated regime. Choosing uniform priors for all orbital parameters results in equal weighting between all possible phases of the orbit. This is demonstrably not the case from basic orbit physics, which dictates that the planet presents the highest orbital speed during periastron passage (T_o). Thus the probability of catching these long-period companions right at T_o is low, since they spend the least amount of time there throughout their orbits. In the case of well-sampled data covering a large fraction of the orbit, the information contained in the data

itself is sufficient to overcome the choice of prior. However, in the case of minimally sampled data, which corresponds typically to linear motion of the planet without measurable higher-order motion such as acceleration, landing in the prior-dominated regime can result in unintended effects. One such example is that astrometric systematics could be interpreted by the fitter as rapid acceleration, hence leading to a best fit that is near periastron. This known bias caused by using uniform priors warranted a different approach to priors when it came to orbit fitting. Observable-based priors (O'Neil et al. 2019) provided such an approach, where the uniformity was in the orbital observables rather than in the orbital parameters. These priors decrease the bias toward high eccentricities and periastron passage during observations, effectively by down-weighting the likelihood of an orbital fit that has T_o near the time of observations. While it is the case that proper approaches to prior definition in Bayesian statistics is a matter of debate, it is important to recognize that in the prior-dominated regime, as we are here, prior choices have measurable consequences in the posteriors, and mitigation of biases is desirable.

Differences in eccentricity posteriors of some of the objects in our sample are indeed noticed when it comes to comparing these two different priors—in particular for HR 2562 b, HD 1160 b, HD 49197 b, HIP 65426 b, and PZ Tel b (for corner plots of these objects in comparison to uniform priors, see Appendix A). In some cases, the long tail of high eccentricities completely disappears (e.g., HD 1160 b) when using observable priors. This is particularly important given our simulation showing that the system only remains stable if HD 1160 b has an eccentricity of < 0.9. Indeed, when RV data is added to HD 1160 b's orbital fit with uniform priors, this is validated—we see a significant shift in its eccentricity posteriors to lower eccentricities, more consistent with what observable priors obtained with an astrometry-only solution. Stability arguments have been successfully used in other cases to help inform the orbital parameters of directly imaged planets, and represent a powerful means of constraint beyond astrometry alone (e.g., Wang et al. 2018).

Period = 200 years, 15% of Orbital Coverage (Observable Priors)
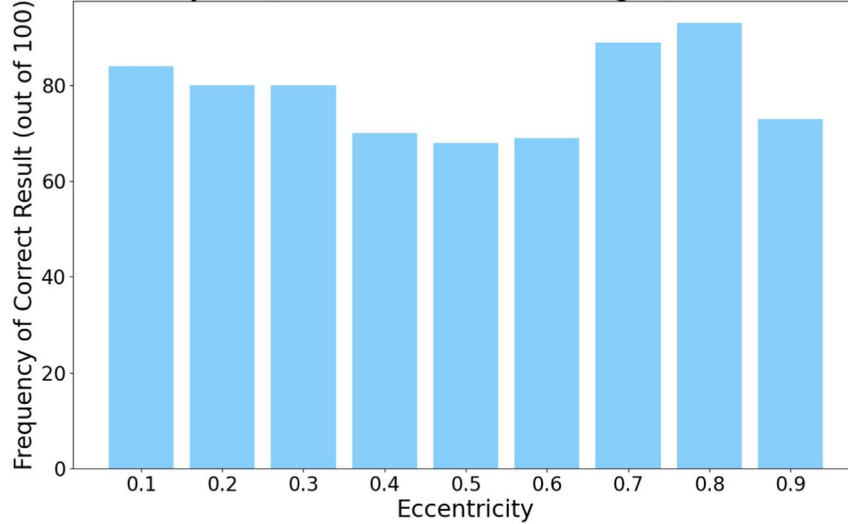
Period = 200 years, 15% of Orbital Coverage (Uniform Priors)
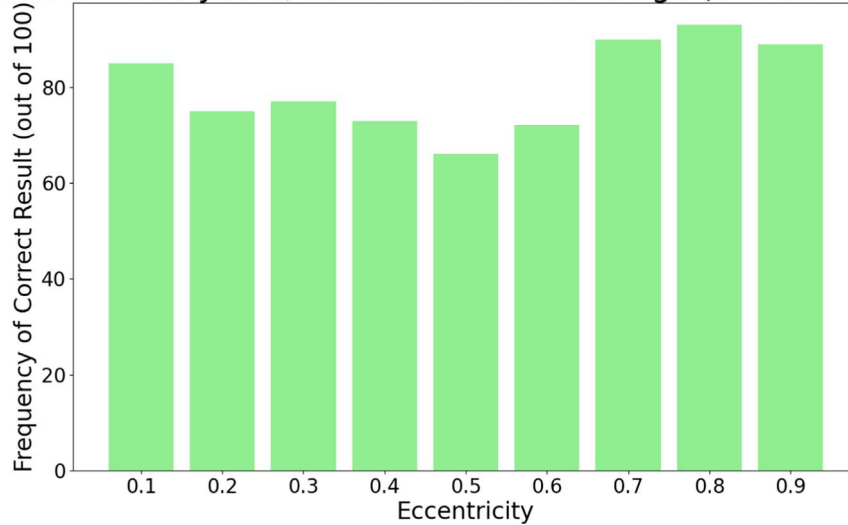
Figure 13. The bar plot of how many successful tries (i.e., true parameters are within 1σ of posterior distribution) we obtain as a function of eccentricity for observable and uniform priors. For 15% of the orbital period in coverage, all of the eccentricity values from 0.1–0.9 have over 68 of the 100 trials considered successful.

5.2. Population Results

Given the major shift in many of the posteriors using observable-based priors, we expected some change in the population distribution from the combined data set. While the specific values of α and β are different from those of Bowler et al. (2020), the overall result is very similar—a nearly uniform distribution, but with a lower incidence of high-eccentricity orbits. Since we did not include all planets from the same multiplanet system in the sample (but rather chose one as the system's "representative") due to the likely preference that multiple planet systems have for lower eccentricities due to stability requirements (Wright & Howard 2009), it is possible that inclusion of these objects (such as HR 8799 b,d,e) could have yielded a population eccentricity distribution with a stronger preference for lower eccentricities. Overall, since the distributions are statistically consistent with each other, we can conclude that current data yields an eccentricity distribution that is largely flat with eccentricity.

5.3. Planets and Brown Dwarfs

Given the fact that the sample size is small and some of the posteriors are prior-dominated, care must be taken when interpreting parameter-based subdivisions of the sample. This is exemplified when we separate the sample by mass into "planets" and "brown dwarfs" (i.e., low- and high-mass objects), as we have three objects (HR 2562 b, κ And b, and β Pic b) that fall into a "boundary" or "intermediate"-mass classification—objects whose mass estimates allow for placement in both classifications. In such cases, we tested placing them in either population to see if results would change. Indeed, placing κ And b and HR 2562 b into the planet population yields completely different results from placing them into the brown dwarf population. Given these results, we conclude the uncertainties in both model-derived masses and individual eccentricity distributions are too large to allow us to distinguish between different populations as a function of mass. This means that at this time, we cannot use eccentricities to say that different formation pathways are underway for substellar

companions above and below $\sim$15 $M_{\rm Jup}$. We note again that the distinction between populations at this mass boundary is not particularly meaningful from a formation perspective, but rather is a useful "breakpoint" to explore these possibilities.

5.4. Minimal Orbital Coverage

Since we are mostly in the prior-dominated regime and there were major changes in posteriors with only a small addition of data, it is important to have some handle on how much data is needed to begin to make meaningful population distributions for directly imaged planets. Our approach here, to look at when we have enough orbital coverage for the eccentricity distribution to cover the true value in simulated data, is one possible way to answer that question. Our finding of 15% coverage is valid for both observable-based and model-based, or uniform, priors. The results converge at that point, suggesting that ultimately the distinction between these two prior sets really only matters for interpreting results in the prior-dominated regime. However, this is not the only possible set of simulations that should be conducted to get a firm handle on the necessary orbital phase coverage. For instance, we did not consider the role of some of the orbital parameters, such as inclination, in defining the needed coverage. Edge-on orbits are often more quickly constrained than face-on, suggesting that this parameter is important to consider. Furthermore, we did not explore, in depth, the role that true time from periastron plays in the defining of meaningful posteriors. Instead, we take 15% as a useful guideline for a general orbit where the companion is not close to periastron, which should encompass the majority of real systems.

As noted above, the average percent coverage of our sample is 7.4%, with most objects having astrometry spanning less than 10% of the orbital period. Given these results, we conclude again that the undersampling of the orbital period for each individual object in our sample coupled with our small sample size does not allow us to affirm that planets and brown dwarfs have different formation pathways. Until the orbits of these objects are well-sampled enough to provide meaningful posteriors, the eccentricity of the population of directly imaged substellar companions remains essentially unconstrained.

6. Conclusion

The main findings of this study are as follows:

1. We derive new orbital parameter posteriors for a set of 21 directly imaged substellar companions using observable-based priors.
2. Several companions have resulting eccentricity distributions that change significantly from previous results. The inclusion of RV data points or new astrometry in the orbit fitting process shifts the resulting posteriors for both observable-based and uniform prior fits.
3. We derive a population-level eccentricity distribution for the 21 companions and obtain shape parameters $\alpha = 1.09^{+0.30}_{-0.22}$ and $\beta = 1.42^{+0.33}_{-0.25}$. These values are consistent with Bowler et al.'s (2020) parameters obtained using uniform priors, but with a lower incidence of high-eccentricity objects.
4. Separating the population into "giant planets" and "brown dwarfs" produces different results depending on

where intermediate-mass objects are placed. This result implies that our current sample size and large uncertainties may not be sufficient to determine whether these objects do in fact present distinct eccentricity populations.
5. From our orbital coverage simulations, we find that one generally needs 15% orbital period coverage to obtain a reliable posteriors on eccentricity, period, and T_o posterior .

Following the conclusions of this work, the addition of new astrometry or RV points for directly imaged companions can help further constrain the eccentricity posteriors of directly imaged companions to reliable intervals. This can in turn allow for more robust eccentricity distributions at a population level.

Appendix A
Corner Plots with Uniform- versus Observable-based Priors

We present in this section the corner plot comparisons between the orbital eccentricities of HD 1160 b (Figures 14 and 15), HD 49197 b (Figure 16), HR 2562 b (Figure 17), HIP 65426 b (Figure 18), and PZ Tel b (Figure 19) when evaluated using uniform- and observable-based priors. We choose these specific objects because, when fit with uniform priors, they present the high-eccentricity bias discussed in Sections 1 and 3.1. When fit with observable-based priors, however, this bias appears to be mostly suppressed.
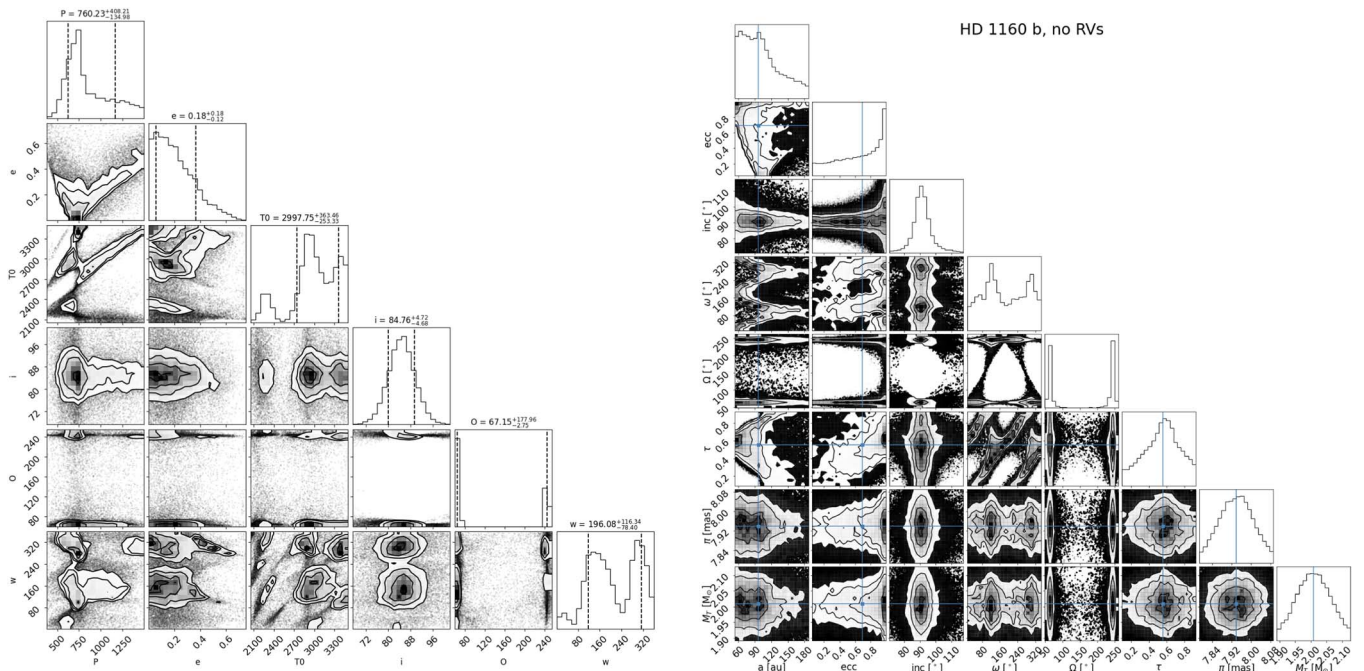
Figure 14. The HD 1160 b orbital parameter corner plots using observable-based priors (left) and uniform priors (right). For this plot, both priors had only astrometry measurements. For observable priors, the columns represent, respectively, the period (P; in years), the eccentricity (e), the epoch of periastron passage (T_0; in years), the inclination (i; in degrees), longitude of ascending node (Ω; in degrees), and argument of periapsis (ω; in degrees). For uniform priors, the columns represent, respectively, the semimajor axis (a; in astronomical unit), the eccentricity (e), the inclination (i; in degrees), the argument of periapsis (ω; in degrees), the longitude of ascending node (Ω; in degrees), the epoch of periastron passage (τ), the distance of the system (π; in milliarcseconds), and the system mass (M; in $M_\odot$).
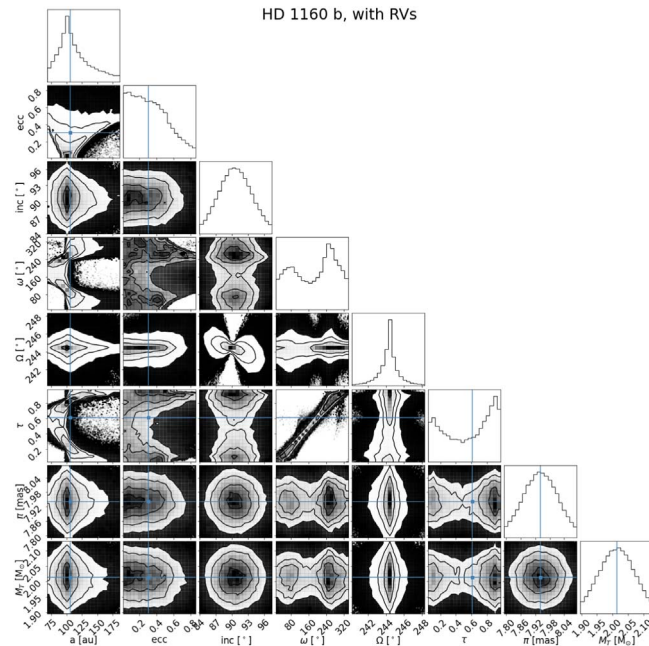
Figure 15. Uniform priors corner plot for HD 1160 b with two RV points added.
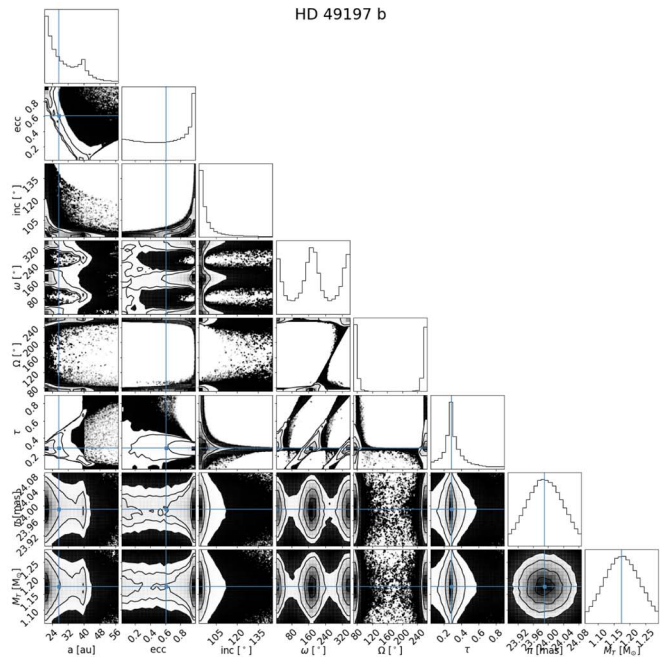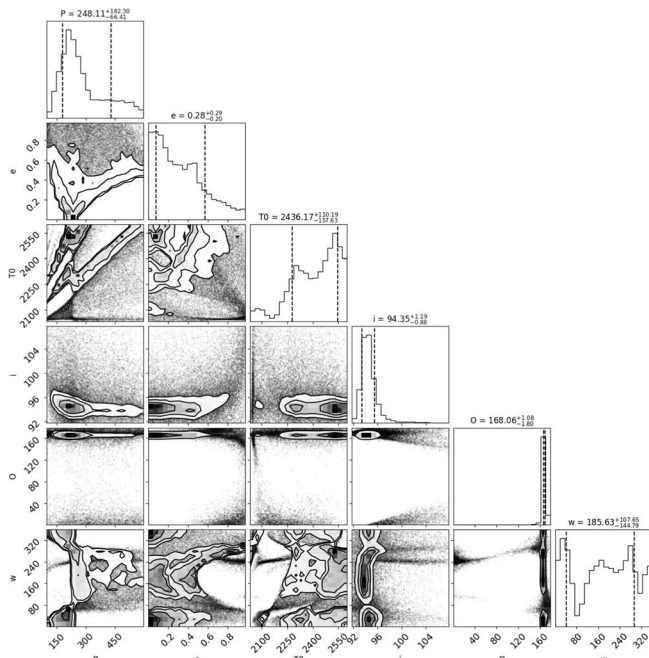
Figure 16. Same as Figure 14, but for HD 49197 B.
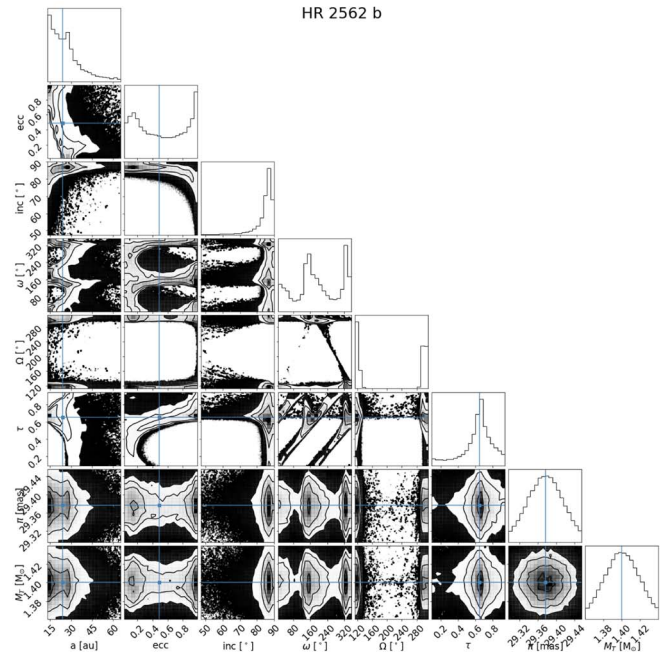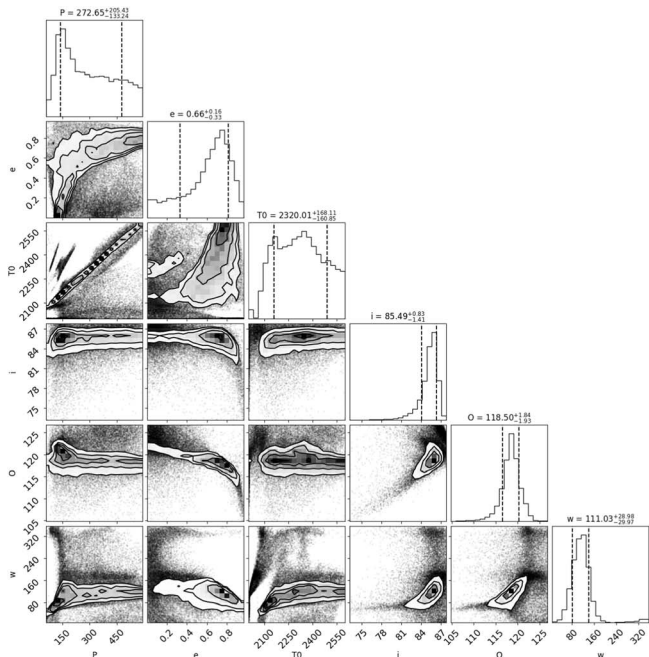
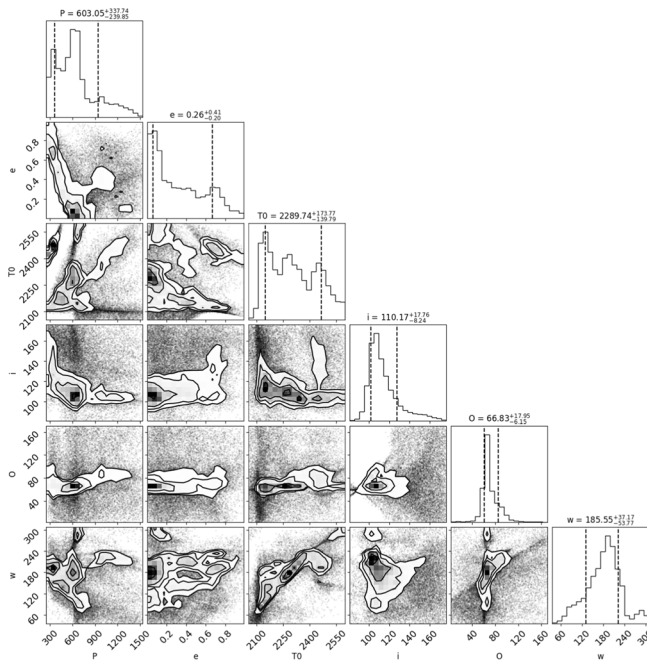**Figure 17.** Same as Figure 14, but for HR 2562 B.
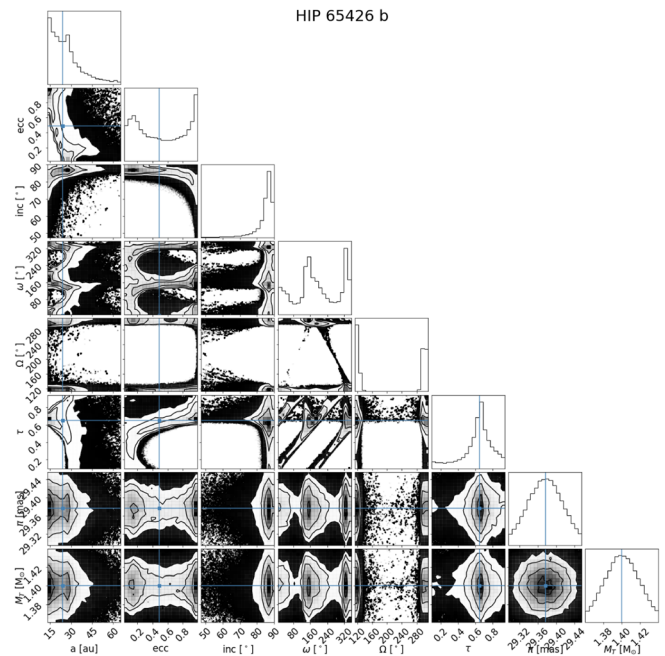
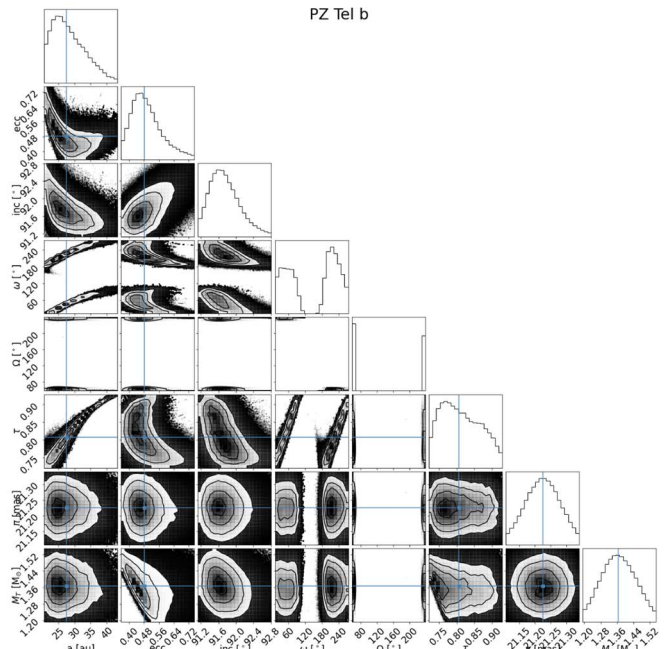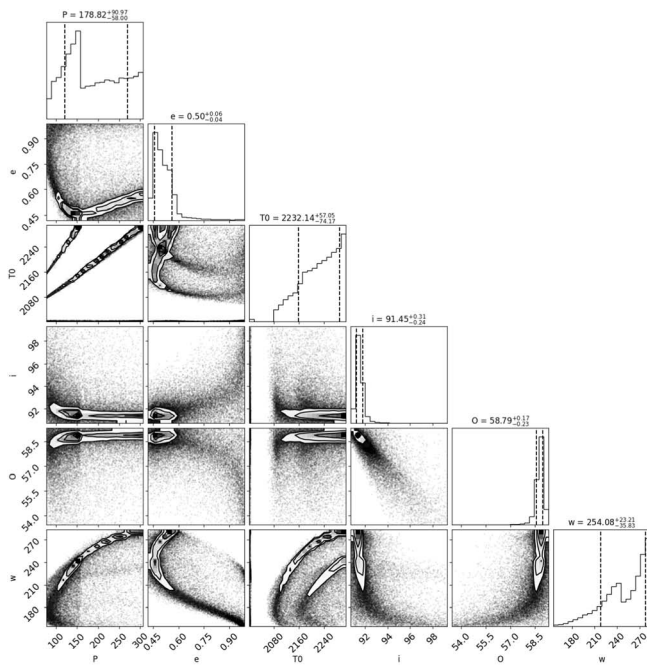**Figure 18.** Same as Figure 14, but for HIP 65426 B.

Figure 19. Same as Figure 14, but for PZ Tel B. Both fits include the 2018 epoch from Table 2. See discussion on this result in Section 4.1.2.

Appendix B
Calculating $\mathcal{P}$

Here we show an example of the calculation to obtain our "consistency parameter" $\mathcal{P}$, defined as the p-value, for two Beta probability distributions. We begin with two Beta distributions for different populations, each with their own pairs of (α_1, β_1) and (α_2, β_2) from their fits. We then sample pairs from each distribution and compute $\delta\alpha = \alpha_2 - \alpha_1$ and $\delta\beta = \beta_2 - \beta_1$ for each iteration. An example of this method for our entire population distribution compared with the whole population minus the object 1RXS0342+1216 B is shown in Figure 20(a). However, this is merely a sample from our distributions, and not a 2D PDF that we can evaluate. So we obtain a Gaussian kernel of this sample, shown in Figure 20(b).

Now with the Gaussian kernel, we are able to integrate the 2D distribution of $(\delta\alpha, \delta\beta)$ inside the contour of constant density that goes through the origin. This allows us to obtain $\mathcal{P}$, which gives us an estimation of how consistent or inconsistent two Beta distributions are.
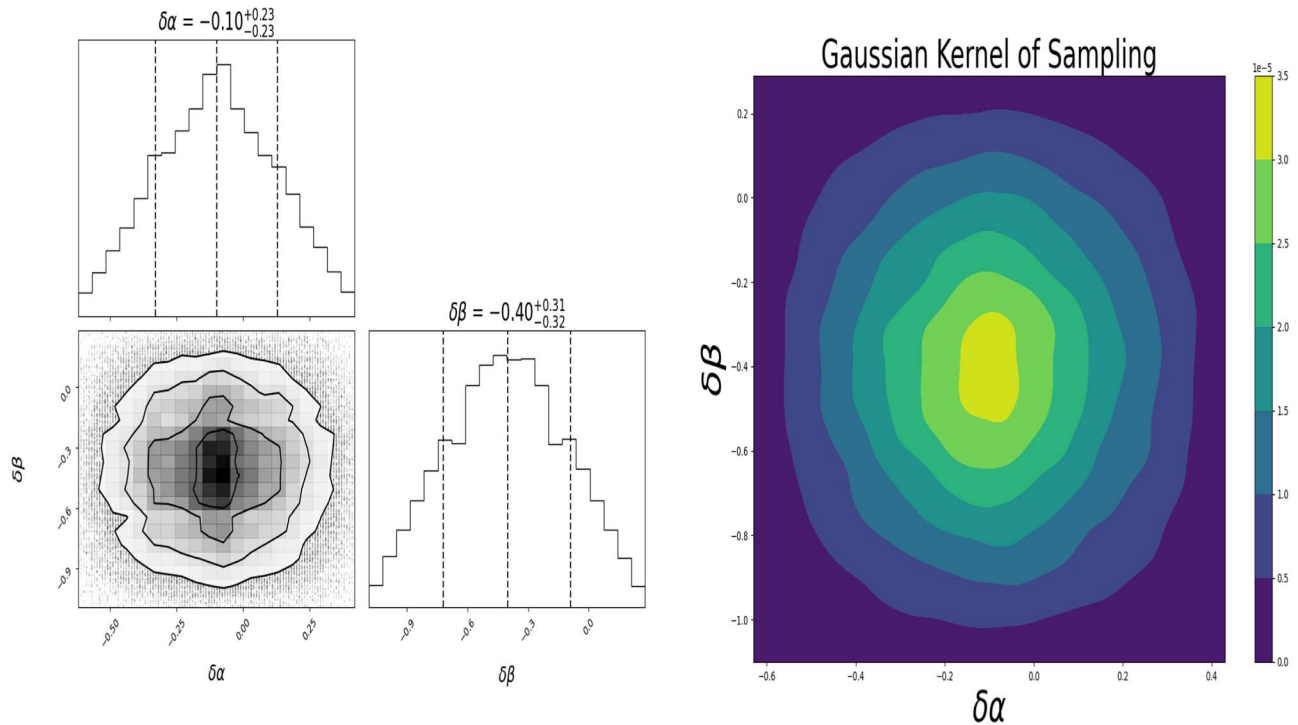

Figure 20. Sample of $\delta\alpha$ and $\delta\beta$ for our distributions with the whole population compared to the distributions with the whole population not including 1RXS0342 +1216 B (a). Gaussian kernel fit to the contour of our sampling (b). From this kernel, we integrate the distribution outside the contour of constant density that goes through the origin.

Appendix C
Individual Corner Plots

The corner plots obtained from Efit5 with observable-based priors for the 21 individual objects are presented in Figure 21.
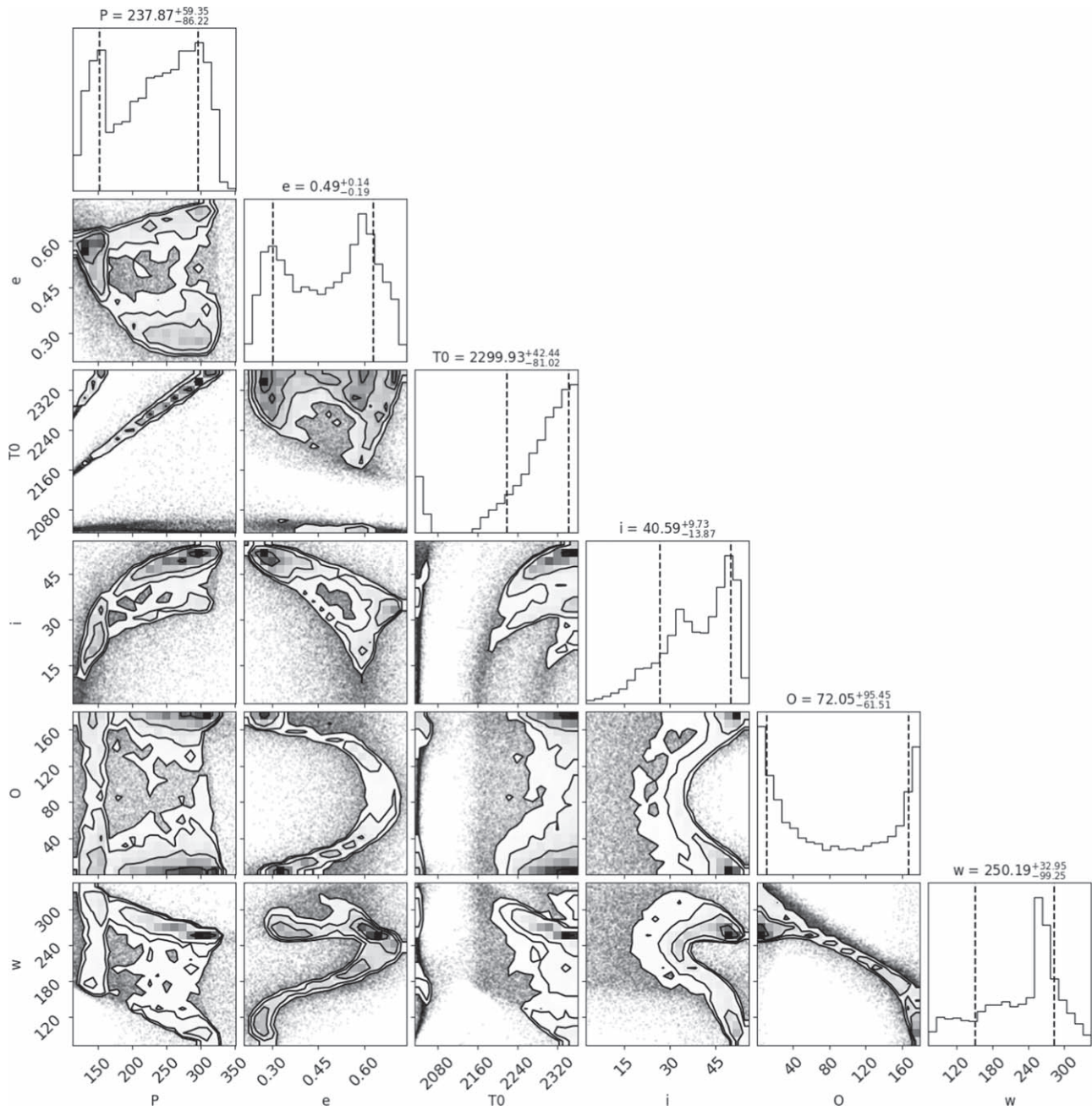
Figure 21. Corner plot for Gl 758 b from Efit5 with observable-based priors. The complete figure set (21 images) is available.

(The complete figure set (21 images) is available.)

ORCID iDs

Clarissa R. Do Ó ● https://orcid.org/0000-0001-5173-2947
Kelly K. O'Neil ● https://orcid.org/0000-0003-2400-7322
Quinn M. Konopacky ● https://orcid.org/0000-0002-9936-6285
Tuan Do ● https://orcid.org/0000-0001-9554-6062
Jean-Baptiste Ruffio ● https://orcid.org/0000-0003-2233-4821
Andrea M. Ghez ● https://orcid.org/0000-0003-3230-5055

References

Bell, C. P. M., Mamajek, E. E., & Naylor, T. 2015, MNRAS, 454, 593
Benisty, M., Bae, J., Facchini, S., et al. 2021, ApJL, 916, L2
Beust, H., Bonnefoy, M., Maire, A.-L., et al. 2016, A&A, 587, A89
Biller, B. A., Liu, M. C., Wahhaj, Z., et al. 2010, ApJL, 720, L82
Bitsch, B., & Kley, W. 2010, A&A, 523, A30
Blunt, S., Wang, J. J., Angelo, I., et al. 2020, AJ, 159, 89
Bodenheimer, P., D'Angelo, G., Lissauer, J. J., Fortney, J. J., & Saumon, D. 2013, ApJ, 770, 120
Bonnefoy, M., Perraut, K., Lagrange, A.-M., et al. 2018, A&A, 618, A63
Bottom, M., Wallace, J. K., Bartos, R. D., Shelton, J. C., & Serabyn, E. 2016, MNRAS, 464, 2937
Bowler, B. P., Blunt, S. C., & Nielsen, E. L. 2020, AJ, 159, 63
Bowler, B. P., Dupuy, T. J., Endl, M., et al. 2018, AJ, 155, 159
Bowler, B. P., Liu, M. C., Shkolnik, E. L., & Tamura, M. 2014, ApJS, 216, 7
Bowler, B. P., Shkolnik, E. L., Liu, M. C., et al. 2015, ApJ, 806, 62
Brandt, T. D., Dupuy, T. J., & Bowler, B. P. 2019, AJ, 158, 140
Brandt, T. D., Dupuy, T. J., Bowler, B. P., et al. 2020, AJ, 160, 196
Bryan, M. L., Bowler, B. P., Knutson, H. A., et al. 2016, ApJ, 827, 100
Byrne, P. B., Doyle, J. G., & Menzies, J. W. 1985, MNRAS, 214, 119
Carson, J., Thalmann, C., Janson, M., et al. 2013, ApJL, 763, L32
Carter, A. L., Hinkley, S., Kammerer, J., et al. 2022, arXiv:2208.14990
Chatterjee, S., Ford, E. B., Matsumura, S., & Rasio, F. A. 2008, ApJ, 686, 580
Chauvin, G., Desidera, S., Lagrange, A.-M., et al. 2017a, A&A, 605, L9
Chauvin, G., Desidera, S., Lagrange, A.-M., et al. 2017b, A&A, 605, L9
Chauvin, G., Gratton, R., Bonnefoy, M., et al. 2018, arXiv:1801.05850
Chauvin, G., Lagrange, A.-M., Beust, H., et al. 2012, A&A, 542, A41
Cheetham, A. C., Samland, M., Brems, S. S., et al. 2019, A&A, 622, A80
Cincotta, P. M., Giordano, C. M., & Simó, C. 2003, PhyD, 182, 151
Crepp, J. R., Gonzales, E. J., Bechter, E. B., et al. 2016, ApJ, 831, 136
Crepp, J. R., Johnson, J. A., Howard, A. W., et al. 2014, ApJ, 781, 29
Crepp, J. R., Rice, E. L., Veicht, A., et al. 2015, ApJL, 798, L43
Currie, T., Brandt, T. D., Uyama, T., et al. 2018, AJ, 156, 291
Currie, T., Thalmann, C., Matsumura, S., et al. 2011, ApJL, 736, L33
De Rosa, R. J., Nguyen, M. M., Chilcote, J., et al. 2020, JATIS, 6, 015006
Delorme, P., Schmidt, T., Bonnefoy, M., et al. 2017, A&A, 608, A79
Dodson-Robinson, S. E., Veras, D., Ford, E. B., & Beichman, C. A. 2009, ApJ, 707, 79
Dong, R., & Dawson, R. 2016, ApJ, 825, 77
Feroz, F., & Hobson, M. P. 2008, MNRAS, 384, 449
Feroz, F., Hobson, M. P., & Bridges, M. 2009, MNRAS, 398, 1601
Franson, K., Bowler, B. P., Brandt, T. D., et al. 2022, AJ, 163, 50
Garcia, E. V., Currie, T., Guyon, O., et al. 2017, ApJ, 834, 162
Ghez, A. M., Becklin, E., Duchjne, G., et al. 2003, ANS, 324, 527
Ginski, C., Schmidt, T. O. B., Mugrauer, M., et al. 2014, MNRAS, 444, 2280
Goldreich, P., & Sari, R. 2003, ApJ, 585, 1024
Grandjean, A., Lagrange, A. M., Beust, H., et al. 2019, A&A, 627, L9
Gray, R. O., Corbally, C. J., Garrison, R. F., et al. 2006, AJ, 132, 161
Haffert, S. Y., Bohn, A. J., de Boer, J., et al. 2019, NatAs, 3, 749
Hartkopf, W. I., McAlister, H. A., & Franz, O. G. 1989, AJ, 98, 1014
Hilditch, R. W. 2001, An Introduction to Close Binary Stars (Cambridge: Cambridge Univ. Press)
Hinkley, S., Lacour, S., Marleau, G. D., et al. 2023, A&A, 671, L5
Hinkley, S., Pueyo, L., Faherty, J. K., et al. 2013, ApJ, 779, 153
Hogg, D. W., Myers, A. D., & Bovy, J. 2010, ApJ, 725, 2166
Janson, M., Bergfors, C., Brandner, W., et al. 2014, ApJS, 214, 17
Janson, M., Hormuth, F., Bergfors, C., et al. 2012, ApJ, 754, 44
Jensen-Clem, R., Millar-Blanchaer, M., Mawet, D., et al. 2016, ApJ, 820, 111

Johansen, A., & Lambrechts, M. 2017, AREPS, 45, 359
Johnson-Groh, M., Marois, C., De Rosa, R. J., et al. 2017, AJ, 153, 190
Jones, J., White, R. J., Quinn, S., et al. 2016, ApJL, 822, L3
Keppler, M., Benisty, M., Müller, A., et al. 2018, A&A, 617, A44
Kipping, D. M. 2013, MNRAS, 434, L51
Kley, W., & Nelson, R. P. 2012, ARA&A, 50, 211
Konopacky, Q. M., Marois, C., Macintosh, B. A., et al. 2016a, AJ, 152, 28
Konopacky, Q. M., Rameau, J., Duchêne, G., et al. 2016b, ApJL, 829, L4
Konopacky, Q. M., Thomas, S. J., Macintosh, B. A., et al. 2014, Proc. SPIE, 9147, 914784
Kuzuhara, M., Tamura, M., Kudo, T., et al. 2013, ApJ, 774, 11
Lacour, S., Wang, J. J., Rodet, L., et al. 2021, A&A, 654, L2
Lagrange, A.-M., Boccaletti, A., Langlois, M., et al. 2019, A&A, 621, L8
Liu, M. C., Fischer, D. A., Graham, J. R., et al. 2002, ApJ, 571, 519
Lodato, G. 2008, NewAR, 52, 21
Lucy, L. B. 2014, A&A, 563, A126
Macintosh, B., Graham, J. R., Barman, T., et al. 2015, Sci, 350, 64
Maire, A.-L., Bonnefoy, M., Ginski, C., et al. 2016, A&A, 587, A56
Maire, A.-L., Molaverdikhani, K., Desidera, S., et al. 2020, A&A, 639, A47
Maire, A.-L., Rodet, L., Cantalloube, F., et al. 2019, A&A, 624, A118
Maire, A.-L., Rodet, L., Lazzoni, C., et al. 2018, A&A, 615, A177
Mamajek, E. E., & Bell, C. P. M. 2014, MNRAS, 445, 2169
Mamajek, E. E., & Hillenbrand, L. A. 2008, ApJ, 687, 1264
Marois, C., Zuckerman, B., Konopacky, Q. M., Macintosh, B., & Barman, T. 2010, Natur, 468, 1080
Martinez, G. D., Kosmo, K., Hees, A., Ahn, J., & Ghez, A. 2017, in IAU Symp. 322, The Multi-Messenger Astrophysics of the Galactic Centre, ed. R. M. Crocker, S. N. Longmore, & G. V. Bicknell (Cambridge: Cambridge Univ. Press), 239
Mawet, D., David, T., Bottom, M., et al. 2015, ApJ, 811, 103
Mayer, L., Quinn, T., Wadsley, J., & Stadel, J. 2004, ApJ, 609, 1045
Mesa, D., Keppler, M., Cantalloube, F., et al. 2019, A&A, 632, A25
Mesa, D., Vigan, A., D'Orazi, V., et al. 2016, A&A, 593, A119
Meshkat, T., Bailey, V., Rameau, J., et al. 2013, ApJL, 775, L40
Meshkat, T., Bonnefoy, M., Mamajek, E. E., et al. 2015, MNRAS, 453, 2379
Metchev, S., & Hillenbrand, L. 2005, Mem. Soc. Astron. Italiana, 76, 404
Meyer, L., Ghez, A. M., Schödel, R., et al. 2012, Sci, 338, 84
Milli, J., Hibon, P., Christiaens, V., et al. 2016, A&A, 597, L2
Moorhead, A. V., & Adams, F. C. 2008, Icar, 193, 475
Mordasini, C., Alibert, Y., Benz, W., Klahr, H., & Henning, T. 2012, A&A, 541, A97
Mugrauer, M., Röll, T., Ginski, C., et al. 2012, MNRAS, 424, 1714
Müller, A., Keppler, M., Henning, T., et al. 2018, A&A, 617, L2
Nakajima, T., Oppenheimer, B. R., Kulkarni, S. R., et al. 1995, Natur, 378, 463
Nielsen, E. L., De Rosa, R. J., Macintosh, B., et al. 2019, AJ, 158, 13
Nielsen, E. L., De Rosa, R. J., Wang, J. J., et al. 2020, AJ, 159, 71
Nielsen, E. L., Liu, M. C., Wahhaj, Z., et al. 2012, ApJ, 750, 53
Nielsen, E. L., Liu, M. C., Wahhaj, Z., et al. 2014, ApJ, 794, 158
O'Neil, K. K., Martinez, G. D., Hees, A., et al. 2019, AJ, 158, 4
Papaloizou, J. C. B., & Terquem, C. 2006, RPPh, 69, 119
Pearce, T. D., Wyatt, M. C., & Kennedy, G. M. 2015, MNRAS, 448, 3679
Rameau, J., Nielsen, E. L., Rosa, R. J. D., et al. 2016, ApJL, 822, L29
Rein, H., & Tamayo, D. 2015, MNRAS, 452, 376
Romero, C., Milli, J., Lagrange, A.-M., et al. 2021, A&A, 651, A34
Ruffio, J.-B., Horstman, K., Mawet, D., et al. 2023, AJ, 165, 113
Ruffio, J.-B., Macintosh, B., Konopacky, Q. M., et al. 2019, AJ, 158, 200
Serabyn, E., Mawet, D., Bloemhof, E., et al. 2009, ApJ, 696, 40
Snellen, I. A. G., Brandl, B. R., de Kok, R. J., et al. 2014, Natur, 509, 63
Stolker, T., Quanz, S. P., Todorov, K. O., et al. 2020, A&A, 635, A182
Thompson, W., Marois, C., Do, Ó. C. R., et al. 2023, AJ, 165, 29
Van Eylen, V., Albrecht, S., Huang, X., et al. 2019, AJ, 157, 61
Virtanen, P., Gommers, R., Oliphant, T. E., et al. 2020, NatMe, 17, 261
Wagner, K., Follette, K. B., Close, L. M., et al. 2018, ApJL, 863, L8
Wang, J. J., Ginzburg, S., Ren, B., et al. 2020, AJ, 159, 263
Wang, J. J., Graham, J. R., Dawson, R., et al. 2018, AJ, 156, 192
Wang, J. J., Ruffio, J.-B., Morris, E., et al. 2021, AJ, 162, 148
Wilcomb, K. K., Konopacky, Q. M., Barman, T. S., et al. 2020, AJ, 160, 207
Wright, J. T., & Howard, A. W. 2009, ApJS, 182, 205
Wright, J. T., Upadhyay, S., Marcy, G. W., et al. 2009, ApJ, 693, 1084
Xuan, J. W., Wang, J., Ruffio, J.-B., et al. 2022, ApJ, 937, 54
Xuan, J. W., & Wyatt, M. C. 2020, MNRAS, 497, 2096
Yimiao Zhang, S., Duchêne, G., De Rosa, R. J., et al. 2023, arXiv:2302.04893